

Ocean acoustic tomography: Travel time biases

John L. Spiesberger^{a)}

Department of Ocean Engineering, Woods Hole Oceanographic Institution, Woods Hole, Massachusetts 02543

(Received 22 March 1984; accepted for publication 31 July 1984)

The travel times of acoustic rays traced through a climatological sound-speed profile are compared with travel times computed through the same profile containing an eddy field. The exact travel time difference is compared with its constituent terms, one of which is linearly related to the deviation of the sound speed (referenced to the climatological profile) and the others which are nonlinearly related to the deviation. At ranges that are much greater than the eddy scale and for eddy fields whose range-averaged temperature anomaly is small, the numerical results are: (1) the values of the nonlinear terms are insensitive to changes in the positions of the eddies and (2) the nonlinear terms are approximately proportional to the range between the source and receiver and to the square of the eddy anomaly. At a 1084-km range in the east Atlantic at 24°N (36°N) the nonlinear terms can account for 17% (90%) of the exact travel time change where the temperature anomalies associated with the eddies are typically $\pm 0.5^\circ\text{C}$ ($\pm 1^\circ\text{C}$). Linearized inversions (based on the linear estimator of the travel time difference) which use the *exact* travel time differences for data should yield biased results since the average values of the nonlinear terms are not zero. If an *a priori* knowledge of the eddy spectrum is known, the nonlinear terms could be computed for each ray and subtracted from the exact travel time change. It may then be beneficial to use the corrected set of travel time differences in a linear inversion which would require no iteration.

PACS numbers: 43.30.Bp, 43.30.Cq, 92.10.Vz, 43.30.Pc

INTRODUCTION

Experiments^{1,2} in ocean acoustic tomography have been conducted over ranges of the order of 1000 km. It is of interest to determine the precision and resolution with which sound speed, temperature, and density can be mapped at gyre-scale ranges for one-way transmissions.³ Inversions start from a reference sound-speed profile from which deviations are modeled using the difference between travel times of reference and measured ray paths.⁴ At a 300-km range, the travel time differences are nearly linearly related to the sound-speed deviations caused by the mesoscale features which are found over most of the oceans (away from the mesoscale rings which are neighbors of the western boundary currents).⁵ This paper investigates the nature of the forward travel time problem at long ranges subject to a field of mesoscale perturbations which deflect the ray paths in the vertical coordinate. The excess travel time associated with horizontal deflections due to a single eddy has been treated by Munk⁶ and will be discussed later.

In mid-ocean regions below a few hundred meters depth, fluctuations of the ray path are principally caused by temperature fluctuations ($\pm 1^\circ\text{C}$) associated with the eddies. The anomaly of sound speed associated with eddies ($\pm 5\text{ m/s}$) is about 50 times greater than changes of propagation speed associated with the eddy currents ($\pm 0.1\text{ m/s}$). For simplicity, the effects of currents are not discussed here.

The travel time definitions are discussed in Sec. I. The ray tracing is discussed in Sec. II. In order to assess the accuracy of linearizing the relations between the travel time difference and the sound-speed deviation at long ranges

($\sim 1000\text{ km}$), calculations are made for two different eddy fields measured in the eastern Atlantic (Secs. III and IV). Because the nonlinearities are found to be significant for some cases, it is of interest to investigate the relationships between the values of the nonlinearities with the range between source and receiver, the anomaly size associated with the eddies, and the positions of the eddies (Secs. V–VII). An analytical model of the nonlinearities is discussed in Sec. VIII. The results of this model are compared with the results of the numerical simulations in Sec. IX, along with other comments.

I. FORWARD PROBLEM

A. Travel time definitions

The initial or unperturbed travel time for each ray between a fixed acoustic source and receiver is given by

$$T_0 = \int_{\Gamma_0} \frac{ds}{c_0(x,z)}, \quad (1)$$

where c_0 is the initial sound speed and the integral is evaluated along the initial ray path Γ_0 .

The exact perturbed travel time is given by

$$T_1 = \int_{\Gamma_1} \frac{ds}{c_0(x,z) + \delta c(x,z)}, \quad (2)$$

where δc is the perturbation to the initial state and the integral is evaluated along the perturbed ray path Γ_1 . The perturbed path is chosen to be the one which becomes the unperturbed path as the perturbation goes to zero.

The exact travel time change between the initial and perturbed state is

$$\delta T_1 = T_1 - T_0 = \int_{\Gamma_1} \frac{ds}{c_0 + \delta c} - \int_{\Gamma_0} \frac{ds}{c_0}. \quad (3)$$

^{a)} Also a visiting scientist at the Department of Earth, Atmospheric, and Planetary Sciences, Massachusetts Institute of Technology, Cambridge, MA 02139.

Since $\delta c/c_0 \sim 0.003$ for mid-ocean sound-speed perturbations, T_1 can be expanded as

$$T_1 = \int_{r_1} \frac{ds}{c_0} \left[1 - \frac{\delta c}{c_0} + \left(\frac{\delta c}{c_0} \right)^2 - \dots \right], \quad (4)$$

which converges rapidly. δT_1 can now be written as

$$\delta T_1 = \left(\int_{r_1} \frac{ds}{c_0} - \int_{r_0} \frac{ds}{c_0} \right) - \int_{r_1} \frac{ds}{c_0^2} \delta c \left(1 - \frac{\delta c}{c_0} + \dots \right),$$

or

$$\delta T_1 = \delta T_5 - \int_{r_1} \frac{ds}{c_0^2} \delta c \left(1 - \frac{\delta c}{c_0} + \dots \right), \quad (5)$$

where

$$\delta T_5 = \int_{r_1} \frac{ds}{c_0} - \int_{r_0} \frac{ds}{c_0}. \quad (6)$$

The last term in Eq. (5) can be broken into two parts, such as

$$- \int_{r_1} \frac{ds}{c_0^2} \delta c \left(1 - \frac{\delta c}{c_0} + \dots \right) = - \int_{r_0} \frac{ds}{c_0^2} \delta c + \delta T_6. \quad (7)$$

The reason for selecting this decomposition is that the term

$$\delta T_2 = - \int_{r_0} \frac{ds}{c_0^2} \delta c \quad (8)$$

is a linear approximation for the exact time change.⁵ It is linear since δc is linearly related to δT_2 .

δT_6 can be written from Eq. (7) as

$$\delta T_6 = \int_{r_0} \frac{ds}{c_0^2} \delta c - \int_{r_1} \frac{ds}{c_0^2} \delta c + \int_{r_1} \frac{ds}{c_0^2 (c_0 + \delta c)}. \quad (9)$$

The exact travel time change can now be written as

$$\delta T_1 = \delta T_2 + \delta T_5 + \delta T_6. \quad (10)$$

Simpler expressions for δT_1 can be obtained when models are expressed in terms of the index of refraction instead of sound speed. The index of refraction is defined by

$$n(x, z) = \bar{c}/c(x, z), \quad (11)$$

where \bar{c} is a constant. The exact travel time could then be written as

$$\delta T_1 = \delta \tilde{T}_2 + \delta T_5 + \delta \tilde{T}_6, \quad (12)$$

where

$$\delta \tilde{T}_2 = \delta T_2 + \int_{r_0} \frac{ds}{c_0^2 (c_0 + \delta c)}, \quad (13)$$

and

$$\delta \tilde{T}_6 = \delta T_6 - \int_{r_0} \frac{ds}{c_0^2 (c_0 + \delta c)} \quad (14)$$

(Appendix A). For index of refraction models, a linear estimator is

$$\delta \tilde{T}_2 = \frac{1}{\bar{c}} \int_{r_0} ds \delta n(x, z), \quad (15)$$

where

$$\delta n(x, z) = \bar{c}/[c_0 + \delta c(x, z)] - \bar{c}/c_0 \quad (16)$$

is the perturbation to the index of refraction (Appendix A). The nonlinear terms are

$$\delta T_5 = \frac{1}{\bar{c}} \left(\int_{r_1} ds n_0 - \int_{r_0} ds n_0 \right), \quad (17)$$

where

$$n_0(x, z) = \bar{c}/c_0(x, z), \quad (18)$$

and

$$\delta \tilde{T}_6 = \frac{1}{\bar{c}} \left(\int_{r_1} ds \delta n - \int_{r_0} ds \delta n \right) \quad (19)$$

(Appendix A). The nonlinear term δT_5 is the same value regardless of whether the model is expressed in terms of the sound speed or the index of refraction. $\delta \tilde{T}_2$ is a better (worse) estimator of δT_1 than δT_2 by the amount

$$\int_{r_0} \frac{ds}{c_0^2 (c_0 + \delta c)}, \quad (20)$$

when $\delta \tilde{T}_6$ is greater (less) than zero.

An enlightening interpretation of δT_5 and $\delta \tilde{T}_6$ can be made by expanding these terms about the unperturbed path using the calculus of variations. The expansions are carried out in terms of two functions. The first function is an arbitrary displacement $\eta(x)$ from the unperturbed ray path. The second function is the derivative of η with respect to the range coordinate x . The *general* expansions are carried out through the first two nonvanishing orders in these variables after careful consideration of Fermat's principle (Appendix A). When the initial index of refraction profile is a function of the depth coordinate only, the expressions for δT_5 and $\delta \tilde{T}_6$ are simpler and are shown here. The *first* nonvanishing terms in the expansions are

$$\begin{aligned} \delta T_5 = & \frac{1}{2\bar{c}} \int_0^R dx \eta^2 \left[\frac{1}{\cos \theta_0} \frac{\partial^2 n_0}{\partial z^2} + 3 \cos \theta_0 \left(\frac{\partial \cos \theta_0}{\partial x} \right)^2 n_0 - \frac{\partial \sin \theta_0}{\partial x} \frac{\partial n_0}{\partial z} + \frac{3 \cos^2 \theta_0}{2} \frac{\partial^2 \cos \theta_0}{\partial x^2} n_0 + \dots \right] \\ & - \frac{1}{2\bar{c}} \int_0^R dx n_0 \cos^3 \theta_0 \eta \frac{d^2 \eta}{dx^2} + \dots \end{aligned} \quad (21)$$

and

$$\delta \tilde{T}_6 = \frac{-1}{\bar{c}} \int_0^R dx \eta \left(\frac{-1}{\cos \theta_0} \frac{\partial (\delta n)}{\partial z} + \frac{\partial \sin \theta_0}{\partial x} \delta n + \sin \theta_0 \frac{\partial (\delta n)}{\partial x} + \dots \right). \quad (22)$$

TABLE I. Typical sizes for the terms in Eqs. (21) and (22) (Appendix B). The terms for $\delta\tilde{T}_6$ are evaluated for a mesoscale eddy whose maximum temperature anomaly is $\delta\theta$ ($^{\circ}\text{C}$).

Term	Above axis	Axis	Below axis
(1) $\frac{\eta^2}{2\bar{c} \cos \theta_0} \frac{\partial^2 n_0}{\partial x^2}$ (s/km)	$-0.03\eta^2$	$-0.01\eta^2$	$-0.001\eta^2$
(2) $\frac{n_0 \cos^3 \theta_0}{2\bar{c}} \eta \frac{d^2 \eta}{dx^2}$	$-0.03\eta^2$	$-0.03\eta^2$	$-0.03\eta^2$
(3) $\frac{\eta^2 \cos^2 \theta_0}{4\bar{c}} \frac{\partial^2 \cos \theta_0}{\partial x^2} n_0$	$-0.002\eta^2$	$-0.002\eta^2$	$-0.0002\eta^2$
(4) $\frac{\eta^2}{2\bar{c}} \frac{\partial \sin \theta_0}{\partial x} \frac{\partial n_0}{\partial z}$	$\pm 0.0003\eta^2$	0	$\pm 0.00005\eta^2$
(5) $\frac{\eta^2 \cos \theta_0}{2\bar{c}} \left(\frac{\partial \cos \theta_0}{\partial x} \right)^2 n_0$	$0.00001\eta^2$	$0.00001\eta^2$	$0.000001\eta^2$
(6) $\frac{\eta}{\bar{c} \cos \theta_0} \frac{\partial(\delta n)}{\partial z}$	$0.004\eta\delta\theta$	$0.002\eta\delta\theta$	0
(7) $\frac{\eta}{\bar{c}} \frac{\partial \sin \theta_0}{\partial x} \delta n$	$0.00007\eta\delta\theta$	$0.00003\eta\delta\theta$	0
(8) $\frac{\eta \sin \theta_0}{\bar{c}} \frac{\partial(\delta n)}{\partial x}$	$0.00005\eta\delta\theta$	$0.00002\eta\delta\theta$	0

The range between source and receiver is R . In Eqs. (21) and (22), $\eta(x)$ is taken to be the vertical distance between the unperturbed and perturbed ray paths given by

$$\eta(x) = z[\Gamma_1(x)] - z[\Gamma_0(x)]. \quad (23)$$

The vertical coordinate z is positive upwards and the angle θ is measured with respect to the horizontal and is positive upwards. The functions in the integrands of Eqs. (21) and (22) with the subscripts equal to zero are evaluated along the unperturbed ray path. The function δn is also evaluated along the unperturbed path.

The contributions to δT_5 arise from functions which depend on the initial index of refraction profile and initial ray path multiplied by the vertical separation of perturbed and unperturbed ray paths and/or higher-order derivatives of the separation. It is independent of the index of refraction perturbation δn in this expansion.

The contributions to $\delta\tilde{T}_6$ arise from functions of the initial index of refraction profile and initial ray path multiplied by the index of refraction perturbation and the vertical separation (or its derivatives) between the perturbed and initial ray paths.

If the perturbed and unperturbed ray paths coincide everywhere, both δT_5 and $\delta\tilde{T}_6$ vanish.

The orders of magnitude for the terms in Eqs. (21) and (22) are estimated in Appendix B and are shown in Table I. According to the estimates, the leading terms are given by

$$\delta T_5 \cong \frac{1}{2\bar{c}} \int_0^R dx \left(\frac{\eta^2}{\cos \theta_0} \frac{\partial^2 n_0}{\partial x^2} - n_0 \cos^3 \theta_0 \eta \frac{d^2 \eta}{dx^2} \right) \quad (24)$$

and

$$\delta\tilde{T}_6 \cong \frac{1}{\bar{c}} \int_0^R dx \frac{\eta}{\cos \theta_0} \frac{\partial(\delta n)}{\partial z}. \quad (25)$$

The expansions about the unperturbed path contain no dynamical information except for the vanishing of the first-order variations in δT_5 which yield Snell's Law (Appendix

A). The expansions are useful in that they explicitly contain the dependence of the nonlinearities in terms of the ray path separation and the index of refraction anomaly. The decomposition of the nonlinear contribution into two terms is made because δT_5 only depends explicitly on geometrical changes, whereas $\delta\tilde{T}_6$ depends on products of geometrical changes with fluctuations of the refractive index.

B. Other definitions

For the remainder of this paper, models will be expressed in terms of sound speeds. For acoustic tomography experiments with a single source and receiver separated by a distance much greater than the eddy scale, one may not be able to determine where the eddies are. The experimenter might want to approximate the exact travel time change with the linear expression

$$\delta T_3 = - \int_{\Gamma_0} \frac{\langle \delta c(x,z) \rangle}{c_0^2} ds, \quad (26)$$

which relates the range-averaged sound-speed perturbation $\langle \delta c \rangle$ to changes of travel time.

Measures of the errors of the approximations δT_2 and δT_3 to the exact travel time change δT_1 are

$$e_2 = 100 (\delta T_2 - \delta T_1) / \delta T_1 \quad (27)$$

and

$$e_3 = 100 (\delta T_3 - \delta T_1) / \delta T_1. \quad (28)$$

Departures of e_2 from zero arise from the insistence that δT_2 is evaluated along the unperturbed path Γ_0 and from the contribution due to the term given in Eq. (20). Since δT_2 presumes that the range-dependent perturbation is known, e_2 is strictly a measure of nonlinear effects, which are primarily due to the change in the ray path. Departures of e_3 from zero arise from the insistence that δT_3 is evaluated along the unperturbed ray path and that the sound-speed perturbation is a function of depth only.

II. RAY TRACING

The ray trace program, originally written by C. W. Spofford, is called MPP or the multiple profile program. Sound speed is linearly interpolated in range and depth in specified triangular regions. The sound-speed field is continuous everywhere but the gradient of the sound-speed field is discontinuous at the triangular boundaries. The travel times of the eigenrays are computed to an accuracy of ± 0.1 ms and are required to fall within 1 m of the receiver. In order to achieve this accuracy the ray trace code is computed using 64-bit words on a VAX 11/780.

III. 1084-km RANGE AT 24° N IN THE ATLANTIC

In 1981, a hydrographic section was made at 24° 30' N in the Atlantic having mesoscale resolution (Wunsch and Roemmich). Seventeen of these stations between 44° W and 55° W (stations 186 to 202, respectively) are algebraically averaged and an initial sound-speed profile is computed (Fig. 1).

A source and receiver are placed at axis depth (1.1 km) and are separated by a 1084-km range. Ray identifiers are $\pm N(D)$, where \pm is the ray inclination at the source (positive up from the horizontal), N is the total number of upper plus lower turning points, and D is the upper turning depth in meters. The initial travel times and geometries for seven rays are computed. These rays are 34(233), + 36(364), + 38(437), + 40(559), + 42(612), + 44(661), and + 46(705).

The exact travel times and geometries are then computed for the seven rays through the actual sound-speed profile inferred from the 17 hydrographic stations. Relative to the initial state, the perturbed profile contains eddies whose horizontal scales are 100–200 km and whose sound-speed anomalies are about ± 3 m/s (Fig. 2). Sound speeds can be converted to an equivalent temperature perturbation using

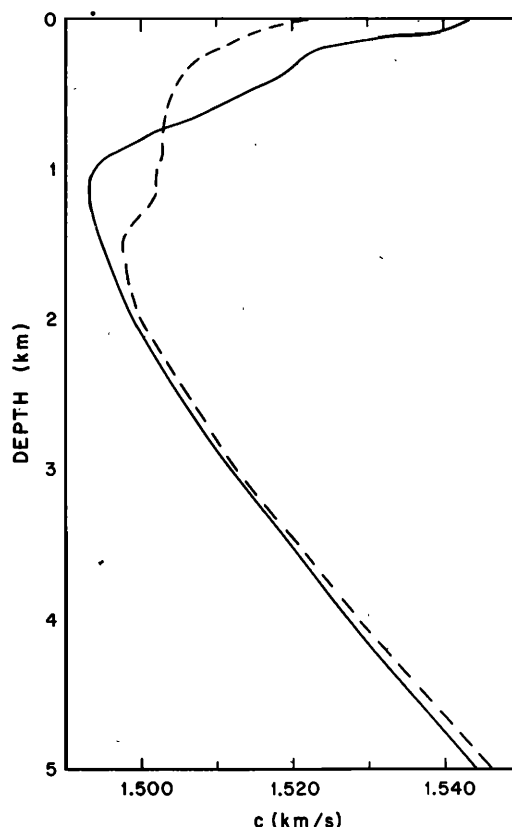


FIG. 1. Average sound-speed profiles in the east Atlantic at 24° N (solid) and 36° N (dashed).

$$\delta c/c = 3.19 \times 10^{-3} \delta \theta. \quad (29)$$

$\delta \theta$ is the temperature perturbation in degrees Celsius. A sound-speed change of ± 3 m/s corresponds to $\pm 0.6^\circ \text{C}$; this is a weak eddy field.

The results of the simulation are:

(a) The amount of the nonlinearity as measured by e_2 is

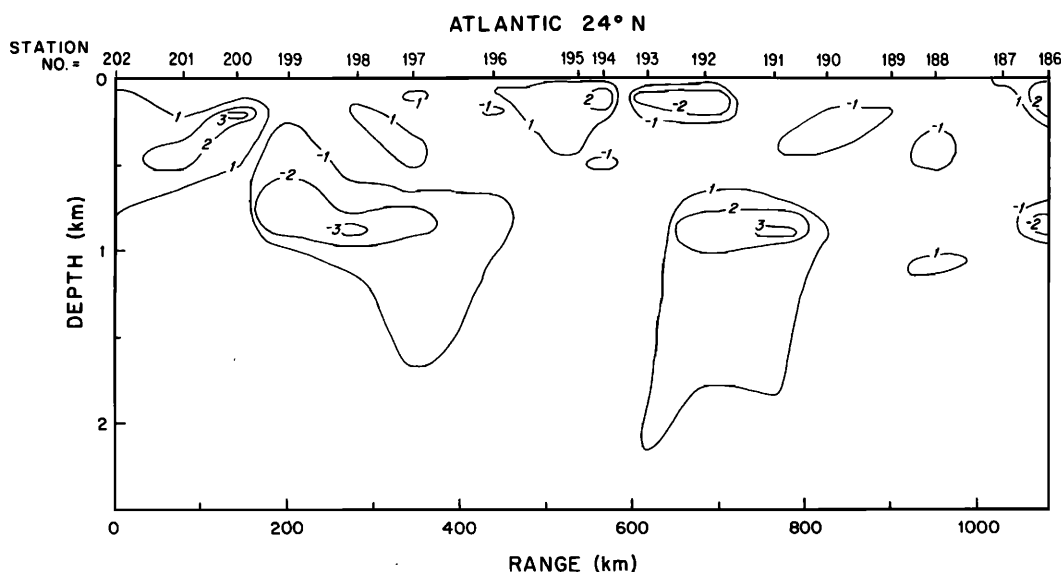


FIG. 2. Sound-speed anomaly (m/s) relative to the average sound-speed profile at 24° N (Fig. 1). The hydrographic data were generously provided by Wunsch and Roemmich.

TABLE II. Results for δT_1 , δT_2 , and δT_3 for a section in the east Atlantic (Fig. 2).

Initial ray	Atlantic 24 °N, 1084-km range				
	δT_1 (ms)	δT_2	δT_3	e_2 (%)	e_3
+ 34 (233)	+ 33.2	+ 27.7	+ 21.1	- 17	- 36
+ 36 (364)	+ 25.1	+ 24.1	+ 20.8	+ 8	- 17
+ 38 (437)	+ 29.1	+ 25.7	+ 23.5	- 12	- 19
+ 40 (559)	+ 29.1	+ 25.6	+ 26.4	- 12	- 9
+ 42 (612)	+ 35.1	+ 34.0	+ 32.3	- 3	- 8
+ 44 (661)	+ 34.9	+ 34.0	+ 37.2	- 3	+ 7
+ 46 (705)	+ 38.4	+ 38.0	+ 39.7	- 1	+ 3

at most - 17% (Table II). δT_2 is a good approximation to the exact travel time change.

(b) The flat rays are more linear than the steep rays (Table II).

(c) δT_2 is usually a better estimator for δT_1 than is δT_3 (Table II).

(d) e_3 , which measures the error of the nonlinearity plus the error due to assuming the sound-speed change as a function of depth only, is as large as - 36% (Table II).

(e) The nonlinear terms δT_5 and δT_6 are usually of opposite signs (Table III).

(f) The magnitude of δT_6 is usually greater than the magnitude of δT_5 (Table III). δT_6 is as large as + 7.2 ms.

The values for δT_3 would be zero if the range average of the sound-speed anomaly vanished at all depths. Because the unperturbed profile is not a range weighted average, δT_3 does not vanish.

The term in Eq. (20) was evaluated numerically and was found to equal about 0.3 ms for all the rays. The linear estimator δT_2 is only slightly different than δT_2 .

The expansions for δT_5 and δT_6 require that the respective integrands are differentiable at all orders. Unfortunately, the sound-speed field used by the ray trace program is not differentiable at the boundaries of the triangular regions. Furthermore, there is no ray program whose sound-speed field is differentiable at all orders and which is capable of tracing rays through realistic range-dependent sound-speed fields. Therefore, it is impossible, in principle, to presently evaluate the various orders of terms in Eqs. (21) and (22) using numerical techniques.

It is possible to calculate the integrands of δT_5 and δT_6 from Eqs. (6) and (9) numerically. The evaluation of these

TABLE III. Results for δT_1 , δT_2 , δT_5 , and δT_6 for a section in the east Atlantic (Fig. 2).

Initial ray	Atlantic 24 °N, 1084-km range				
	δT_1 (ms)	δT_2	δT_5	δT_6	$\delta T_5 + \delta T_6$
+ 34 (233)	+ 33.2	+ 27.7	+ 0.5	+ 5.1	+ 5.6
+ 36 (364)	+ 25.1	+ 24.1	- 2.0	+ 3.0	+ 1.0
+ 38 (437)	+ 29.1	+ 25.7	- 3.0	+ 6.4	+ 3.4
+ 40 (559)	+ 29.1	+ 25.6	- 3.6	+ 7.2	+ 3.6
+ 42 (612)	+ 35.1	+ 34.0	- 0.3	+ 1.4	+ 1.1
+ 44 (661)	+ 34.9	+ 34.0	- 0.2	+ 1.1	+ 0.9
+ 46 (705)	+ 38.4	+ 38.0	+ 0.7	- 0.3	+ 0.4

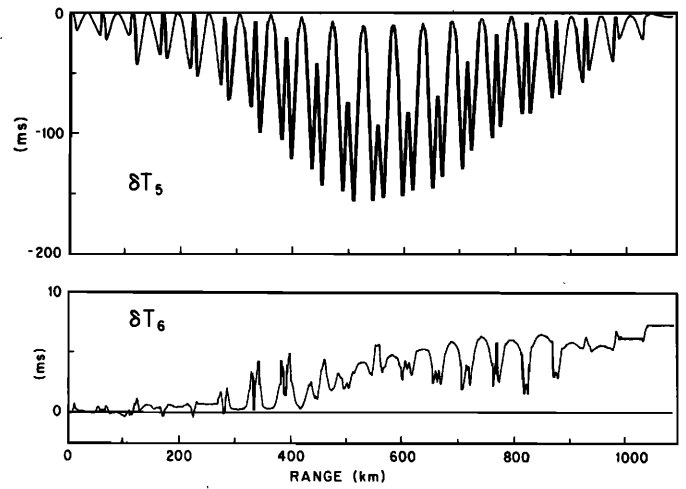


FIG. 3. The growth of the nonlinear terms as a function of range at 24 °N in the east Atlantic for + 40 (559). Note that the vertical scales differ.

integrands does not require the existence of derivatives at all orders, since no expansions have been made with these requirements at this stage. Figure 3 graphs the functions

$$\delta T_5(x) = \int_0^x \frac{d\xi}{\cos \theta_1 c_0(\Gamma_1)} - \int_0^x \frac{d\xi}{\cos \theta_0 c_0(\Gamma_0)} \quad (30)$$

and

$$\delta T_6(x) = \int_0^x \frac{d\xi \delta c(\Gamma_0)}{\cos \theta_0 c_0^2(\Gamma_0)} - \int_0^x \frac{d\xi \delta c(\Gamma_1)}{\cos \theta_1 c_0^2(\Gamma_1)} + \int_0^x \frac{d\xi \delta c^2(\Gamma_1)}{\cos \theta_1 c_0^2(\Gamma_1) [c_0(\Gamma_1) + \delta c(\Gamma_1)]}, \quad (31)$$

for the ray + 40(559). Equations (30) and (31) are the same as

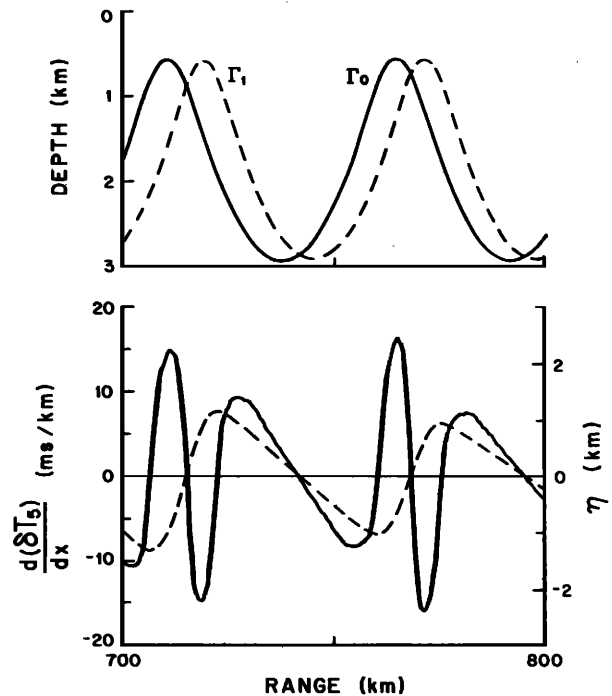


FIG. 4. Upper panel: The initial (Γ_0) and perturbed (Γ_1) ray paths at 24 °N in the east Atlantic for + 40 (559). Lower panel: The integrand of δT_5 (solid) and the path separation (dashed).

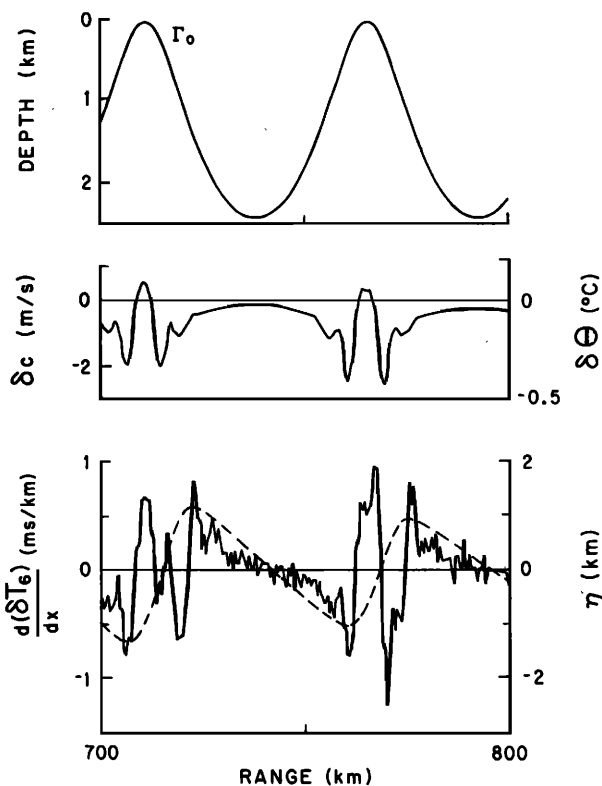


FIG. 5. Upper panel: The initial (Γ_0) ray path at 24°N in the east Atlantic for +40 (559). Middle panel: The sound-speed anomaly along the initial ray path. Lower panel: The integrand of δT_6 (solid) and the ray path separation (dashed).

Eqs. (6) and (9) except for a change of variables from ds , which is an increment of the arc length, to $d\xi$, which is an increment in the range.

δT_5 undergoes large oscillations compared to the size of its value at the final range. Those oscillations are the differences of the travel times accrued by the perturbed and initial ray paths as a function of range. All the upper extrema occur at the ranges at which the ray separation function $\eta(x)$ vanishes. At these ranges the initial and perturbed ray paths cross each other. However, the values of δT_5 at these extrema are *not* the values δT_5 would have if the receiver was at each of these ranges. The perturbed ray path associated with the initial ray path at a 1084-km range is *different* than the perturbed ray path associated with the initial ray path at shorter ranges.

δT_6 increases slowly with range without large oscillations (Fig. 3).

The derivatives of $\delta T_5(x)$ and $\delta T_6(x)$ with respect to the range are the integrands of the integrals and are evaluated numerically. The integrand of δT_5 is oscillatory with an amplitude of about 0.015 s/km and is centered at about zero (Fig. 4). The path separation is also oscillatory with an amplitude of about 1 km. As predicted from the general expansions, the integrand of δT_5 vanishes when the path separation vanishes. The measured amplitude of the integrand compares well with the estimated magnitude for terms (1) and (2) in Table I for $\eta = 1$ km (about 0.03 s/km).

The integrand of δT_6 is oscillatory, having a typical am-

TABLE IV. Change in source angle between perturbed and initial state for a section in the east Atlantic (Fig. 2).

Atlantic 24°N, 1084-km range	
Initial ray	$\theta_1 - \theta_0(^{\circ})$
+34 (233)	-0.075
+36 (364)	+0.077
+38 (437)	-0.048
+40 (559)	+0.13
+42 (612)	+0.0045
+44 (661)	+0.11
+46 (707)	+0.15

plitude of 0.001 s/km (Fig. 5). (The small-scale wiggles are the result of numerical noise.) The integrand of δT_6 is nearly zero [except for the very small contribution due to the term in Eq. (20)] when the path separation vanishes, as predicted by the general expansions. To estimate the size of term (6) in Table I, the values $\eta = 1$ km, $\delta\Theta = 0.4^{\circ}\text{C}$ are taken. Term (6) is then equal to about 0.002 s/km which is about the size of the measured integrand at its maximum values. The measured integrand of δT_6 is small below the sound channel axis as predicted from the expansion for term (6).

The change of the source angle between the perturbed and initial rays is about 0.1° (Table IV). For those interested in using changes of the vertical arrival angle to infer mesoscale variability, a measurement of at least 0.03° precision is required in this region of the ocean to obtain a 10-dB signal-to-noise ratio.

IV. 1084-KM RANGE AT 36°N IN THE ATLANTIC

In 1981, a hydrographic section was made at 36°N in the Atlantic having mesoscale resolution (Wunsch and Roemmich). Seventeen of the stations between 31°W and 19°W (stations 64 to 80, respectively) are algebraically averaged and an initial sound speed-profile is computed (Fig. 1).

A source and receiver are located at axis depth (1.5 km) and are separated by a 1084-km range. The initial travel times and geometries for seven rays are computed. They are +35(71), +34(100), -34(100), +33(231), +32(287), -32(287), and -31(300).

The exact travel times and geometries are then computed for the seven rays through the actual sound-speed profile inferred from the 17 hydrographic stations. Relative to the initial state, the perturbed profile contains eddies whose horizontal scales are about 100 km (smaller than the scale at 24°N). The sound-speed anomalies are about ± 5 m/s (Fig. 6) which correspond to an equivalent anomaly of about $\pm 1^{\circ}\text{C}$.

There is a one-to-one correspondence between perturbed and initial rays for the seven rays. However, the correspondence is not easy to make for rays with flatter trajectories, and so flatter rays are not used in this section. The correspondence is much easier to make for the section at 24°N. The results for the simulation are:

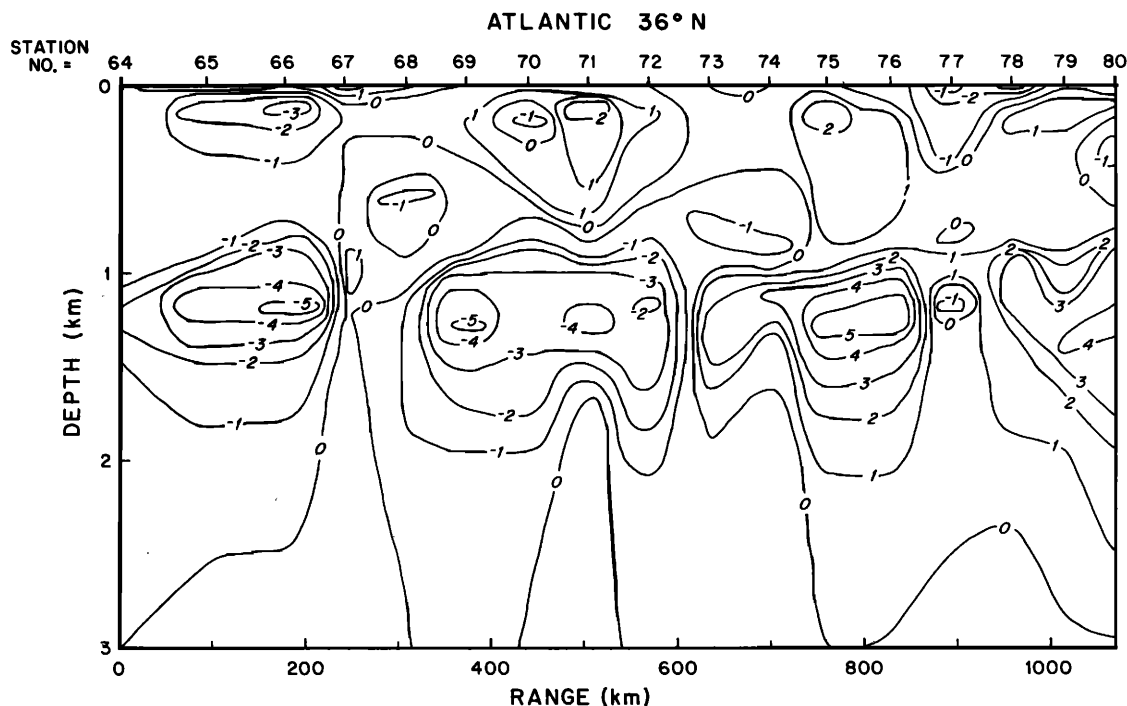


FIG. 6. Sound-speed anomaly (m/s) relative to the average sound-speed profile at 36°N (Fig. 1). The hydrographic data were generously provided by Wunsch and Roemmich.

(a) The amount of nonlinearity, as measured by e_2 , is as large as +90% (Table V). δT_2 is not a good approximation to the exact travel time change.

(b) The flat rays are less linear than the steep rays (Table V).

(c) e_3 is about the same size as e_2 (Table V).

(d) The nonlinear terms δT_5 and δT_6 are of opposite signs (Table VI).

(e) The magnitude of δT_6 is greater than the magnitude of δT_5 (Table VI). δT_6 is as large as -37.8 ms.

The change of the source angle between the perturbed and initial rays is as large at 0.5°, and is typically 0.2° (Table VII).

V. CONSTRUCTION OF THE SIMULATED OCEAN

Since the nonlinearities at 36°N in the eastern Atlantic are significant, it is of interest to study the relationships between the nonlinearities with the total acoustic range, with the size of the eddy anomalies, and with the positions of the

eddies. These relationships are calculated here for an ocean containing a simulated eddy field.

In a previous study, travel times of acoustic rays were computed through an eddy in the Sargasso Sea which was surveyed with CTDs at about 20-km intervals.⁵ The eddy had a length scale of 100 km and had a maximum temperature anomaly of -1.4°C at 700 m depth. The travel times of acoustic rays were also computed through a model of the same eddy. Proceeding in range, the first region was 40 km wide and smoothly joined (in range) an unperturbed sound-speed profile to a sound-speed profile representative of conditions in the eddy. The second region was 60 km wide whose sound-speed profile was independent of range and was the same representation for conditions in the eddy. The third region was the reverse of the first region; it joined the eddy back to the unperturbed state in a range of 40 km. Travel times computed from the three-region model of the eddy were within 2% of those calculated through the fully range-dependent sound-speed profile. The eigenray positions were also very similar for the two cases.

TABLE V. Results for δT_1 , δT_2 , and δT_3 for a section in the east Atlantic (Fig. 2).

Atlantic 36°N, 1084-km range					
Initial ray	δT_1 (ms)	δT_2	δT_3	e_2 (%)	e_3
+ 35 (71)	+ 35.5	+ 40.4	+ 40.2	+ 14	+ 13
+ 34 (100)	+ 41.2	+ 43.3	+ 40.0	+ 5	- 3
- 34 (100)	+ 32.4	+ 37.3	+ 40.0	+ 15	+ 23
+ 33 (231)	+ 47.5	+ 51.5	+ 50.9	+ 8	+ 7
+ 32 (287)	+ 33.2	+ 51.7	+ 51.0	+ 56	+ 54
- 32 (287)	+ 38.9	+ 50.5	+ 51.0	+ 30	+ 31
- 31 (300)	+ 23.9	+ 45.5	+ 50.4	+ 90	+ 111

TABLE VI. Results for a section in the east Atlantic (Fig. 2).

Atlantic 36°N, 1084-km range					
Initial ray	δT_1 (ms)	δT_2	δT_5	δT_6	$\delta T_5 + \delta T_6$
+ 35 (71)	+ 35.5	+ 40.4	+ 5.7	- 10.6	- 4.9
+ 34 (100)	+ 41.2	+ 43.3	+ 3.4	- 5.5	- 2.1
- 34 (100)	+ 32.4	+ 37.3	+ 5.3	- 10.2	- 4.9
+ 33 (231)	+ 47.5	+ 51.5	+ 1.4	- 5.4	- 4.0
+ 32 (287)	+ 33.2	+ 51.7	+ 14.2	- 32.7	- 18.5
- 32 (287)	+ 38.9	+ 50.5	+ 8.1	- 19.7	- 11.6
- 31 (300)	+ 23.9	+ 45.5	+ 16.2	- 37.8	- 21.6

TABLE VII. Change in source angle between perturbed and initial state for a section in the east Atlantic (Fig. 2).

Atlantic 36 °N, 1084-km range	
Initial ray	$\theta_1 - \theta_0(^{\circ})$
+ 35 (71)	+ 0.22
+ 34 (100)	- 0.12
- 34 (100)	+ 0.21
+ 33 (231)	+ 0.27
+ 32 (287)	+ 0.48
- 32 (287)	- 0.11
- 31 (300)	- 0.057

In this paper, eddies will be simulated with the three regions having boundaries 40 km wide and a central region 60 km wide. The principal reason for this is that the simulation works well and it requires much less computation time than a more detailed representation.

The initial, or unperturbed, state is computed from an average of deep hydrographic measurements in the subtropical Pacific near 30 °N and 145 °W (Fig. 7). The initial state does not depend on range and does not contain sound-speed perturbations due to mid-ocean eddies.

The central 60 km of the simulated eddies are computed from the equation⁷

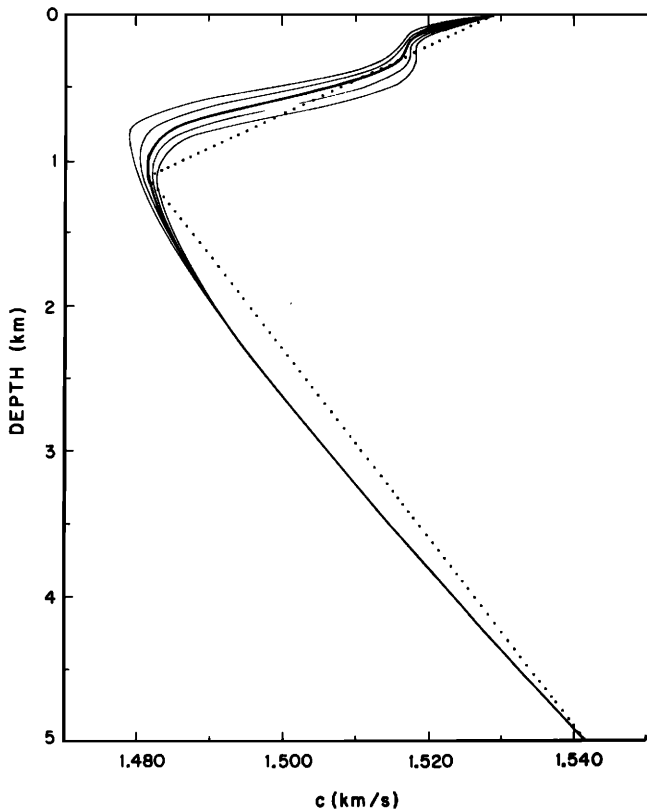


FIG. 7. The average sound-speed profile in the subtropical Pacific (dark solid). The light solid profiles are formed by perturbing the average profile with linear Rossby waves having maximum vertical water displacements of - 100, - 50, + 50, and + 100 m (left to right). A positive displacement means water is displaced upwards. The dotted profile is bilinear and is referred to in Sec. VIII.

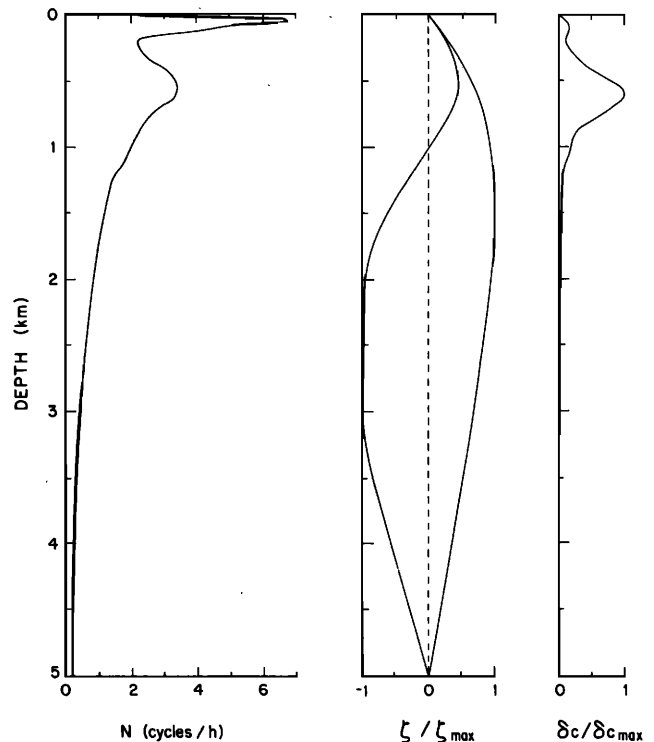


FIG. 8. Left: A climatological buoyancy frequency profile in the subtropical Pacific. Center: The first two linear Rossby wave modes for vertical water displacement (normalized to ± 1). Right: The normalized sound-speed perturbation resulting from the first two Rossby wave modes. Ninety percent of the mean potential energy is in the grave mode and 10% is in the next mode.

$$\frac{d^2 \xi}{dz^2} + \frac{N^2(z)\xi}{\lambda^2} = 0, \quad (32)$$

with boundary conditions

$$\xi(0) = \xi(H) = 0, \quad (33)$$

where ξ is the vertical water displacement from equilibrium (positive upwards), H is the bottom depth, $N(z)$ is the buoyancy frequency, and λ is the eigenvalue. A climatological buoyancy profile near 30 °N and 145 °W in the Pacific is used to solve for the first two Rossby wave modes numerically (Fig. 8). The unperturbed profile is perturbed by these two modes combined such that 90% of the mean potential energy is in the grave mode and the remaining 10% is in the next mode. The resulting sound-speed perturbation has a maximum near 700 m depth (Fig. 8). The sound-speed perturbation is quite small below a kilometer depth because the sound-speed gradient is nearly adiabatic.

VI. 1000-KM RANGE: SUBTROPICAL PACIFIC

The source and receiver are placed at axial depth (1.1 km) for the initial sound-speed profile (Fig. 7) at a 1000-km range. Initial travel times and geometries are computed for seven rays. They are + 36(339), + 38(398), + 40(458), + 42(515), + 44(551), + 46(584), and + 48(618).

The perturbed profile contains three warm eddies and three cold eddies. Each eddy has three regions; two transition zones and a central core as described in Sec. V. The warm eddies are all the same strength; the cold eddies are all

TABLE VIII. Results for the exact (δT_1) and approximate (δT_2 , δT_3) travel time changes for two rays perturbed by linear Rossby wave modes of maximum vertical water displacement of ± 50 m (left) and ± 100 m (right) in the subtropical Pacific. Different realizations correspond to different eddy positions.

Pacific, 1000-km range											
Realization	$\delta T_1(\text{ms})$	$\pm 1^\circ\text{C}$ eddies + 36 (339)			$e_2(\%)$	e_3	Realization	$\delta T_1(\text{ms})$	$\pm 2^\circ\text{C}$ eddies + 36 (339)		
		δT_2	δT_3	$e_2(\%)$					δT_2	δT_3	$e_2(\%)$
1	-6.1	+0.4	-1.4	-107	-77	8	-20.1	+1.4	-2.1	-107	-90
2	-7.3	-3.3	-1.4	-55	-81	9	-22.1	-5.6	-2.1	-75	-90
3	-6.0	+0.3	-1.4	-105	-77	10
4	-10.5	-4.0	-1.4	-62	-87	11	-29.9	-7.2	-2.1	-76	-93
5	-7.3	-3.2	-1.4	-56	-81	12	-22.3	-5.5	-2.1	-75	-91
6	-10.2	-3.7	-1.4	-64	-86	13	-28.7	-6.5	-2.1	-77	-93
7	-12.7	-8.1	-1.4	-36	-89	14	-30.6	-14.9	-2.1	-51	-93
Realization	$\delta T_1(\text{ms})$	$\pm 1^\circ\text{C}$ eddies + 48 (618)			$e_2(\%)$	e_3	Realization	$\delta T_1(\text{ms})$	$\pm 2^\circ\text{C}$ eddies + 48 (618)		
		δT_2	δT_3	$e_2(\%)$					δT_2	δT_3	$e_2(\%)$
1	+19.6	+5.8	+5.6	-70	-71	8	+58.5	+13.8	+13.6	-76	-77
2	+19.1	+5.3	+5.6	-72	-71	9	+57.7	+12.3	+13.6	-79	-76
3	+19.4	+5.6	+5.6	-71	-71	10	+58.1	+13.4	+13.6	-77	-77
4	+19.5	+5.7	+5.6	-71	-71	11	+58.3	+13.7	+13.6	-77	-77
5	+19.1	+5.3	+5.6	-72	-71	12	+57.7	+12.3	+13.6	-79	-76
6	+19.5	+5.8	+5.6	-73	-71	13	+58.3	+13.7	+13.6	-77	-77
7	+18.2	+4.5	+5.6	-75	-69	14	+54.9	+11.6	+13.6	-79	-75

the same strength and have nearly the opposite perturbation as the warm eddies. By demanding that the eddies be nearly of opposite sense, the range-averaged heat content change relative to the initial state is kept small.

Two sets of simulations are done. The first contains eddies whose maximum vertical water displacements are ± 50 m. For these eddies, the maximum sound-speed perturbation is ± 5 m/s at a depth of 600 m. Using Eq. (29), the equivalent temperature anomaly is $\pm 1^\circ\text{C}$.

Seven realizations of the eddy field are constructed by mixing the orders and ranges of the six eddies. Similarly, the second set of simulations contains eddies whose maximum water displacements reach ± 100 m at 600 m depth. These eddies have corresponding perturbations of ± 10 m/s and $\pm 2^\circ\text{C}$ at 600 m depth. Seven realizations of the eddy field are constructed by mixing the orders and ranges.

Exact travel times and geometries are computed for each realization for each of the seven rays. The results for two of the rays, +36(339) and +48(618), are typical. The conclusions are:

(a) The magnitude of the nonlinearity as measured by e_2 is typically 50%–100%. δT_2 is not a good estimator of the exact travel time change (Table VIII).

(b) δT_3 is about as good an estimator for the exact travel time change as is δT_2 (Table VIII).

(c) The nonlinear terms δT_5 and δT_6 are usually of opposite sign (Table IX).

(d) The magnitude of δT_6 is usually greater than the magnitude of δT_5 (Table IX).

(e) The sums of the nonlinear terms for the ± 100 -m eddies usually increase by a factor greater than 2 compared with the ± 50 -m eddies (Table X).

TABLE IX. Contribution to the exact travel time change (δT_1) due to δT_2 , δT_3 , and δT_6 for two rays perturbed by linear Rossby wave modes in the subtropical Pacific.

Pacific, 1000-km range									
Realization	$\pm 1^\circ\text{C}$ eddies + 36 (339)				Realization	$\pm 2^\circ\text{C}$ eddies + 36 (339)			
	$\delta T_1(\text{ms})$	δT_2	δT_3	δT_6		δT_1	δT_2	δT_3	δT_6
1	- 6.1	+ 0.4	+ 6.0	- 12.5	8	- 20.1	+ 1.4	+ 17.7	- 39.2
2	- 7.3	- 3.3	+ 4.3	- 8.3	9	- 22.1	- 5.6	+ 15.5	- 32.0
3	- 6.0	+ 0.3	+ 5.9	- 12.2	10
4	- 10.5	- 4.0	+ 5.8	- 12.3	11	- 29.9	- 7.2	+ 17.4	- 40.1
5	- 7.3	- 3.2	+ 4.4	- 8.5	12	- 22.3	- 5.5	+ 15.8	- 32.6
6	- 10.2	- 3.7	+ 3.8	- 10.3	13	- 28.7	- 6.5	+ 9.5	- 31.7
7	- 12.7	- 8.1	+ 4.6	- 9.2	14	- 30.6	- 14.9	+ 14.2	- 29.9
+ 48 (618)									
1	+ 19.6	+ 5.8	- 9.7	+ 23.5	8	+ 58.5	+ 13.8	- 28.6	+ 73.3
2	+ 19.1	+ 5.3	- 9.8	+ 23.6	9	+ 57.7	+ 12.3	- 30.1	+ 75.5
3	+ 19.4	+ 5.6	- 14.8	+ 28.6	10	+ 58.1	+ 13.4	- 28.4	+ 73.1
4	+ 19.5	+ 5.7	- 9.7	+ 23.5	11	+ 58.3	+ 13.7	- 28.6	+ 73.2
5	+ 19.1	+ 5.3	- 9.8	+ 23.6	12	+ 57.7	+ 12.3	- 29.8	+ 75.2
6	+ 19.5	+ 5.8	- 9.6	+ 23.3	13	+ 58.3	+ 13.7	- 28.7	+ 73.3
7	+ 18.2	+ 4.5	- 9.4	+ 23.1	14	+ 54.9	+ 11.6	- 27.5	+ 70.8

TABLE X. The means, standard deviation, and sums of the nonlinear terms for seven realizations of the eddy field.

Initial ray	Pacific, 1000-km range									
	$\pm 1^\circ\text{C}$ eddies					$\pm 2^\circ\text{C}$ eddies				
	$\delta\bar{T}_5(\text{ms})$	σ	$\delta\bar{T}_6$	σ	$\delta\bar{T}_5 + \delta\bar{T}_6$	$\delta\bar{T}_5$	σ	$\delta\bar{T}_6$	σ	$\delta\bar{T}_5 + \delta\bar{T}_6$
+ 36 (339)	+ 5.0	± 0.9	- 10.	$\pm 2.$	- 5.0	+ 15.	± 3	- 34.	± 4	- 19.
+ 38 (398)	+ 6.3	± 0.7	- 9.5	$\pm 1.$	- 3.2	+ 6.1	± 2	- 19.	± 2	- 13.
+ 40 (458)	- 0.56	± 0.3	- 1.5	± 0.2	- 2.1	- 2.6	± 1	+ 0.37	± 2	- 2.2
+ 42 (515)	- 3.1	± 0.06	+ 6.6	± 0.08	+ 3.5	- 10.	± 1	+ 23.	± 1	+ 13.
+ 44 (551)	- 5.7	± 0.3	+ 10.	$\pm 1.$	+ 4.3	- 26.	± 1	+ 50.	± 2	+ 24.
+ 46 (584)	- 9.1	± 0.1	+ 18.	± 0.2	+ 8.9	- 29.	± 0.7	+ 63.	± 1	+ 34.
+ 48 (618)	- 10.0	$\pm 2.$	+ 24.	$\pm 2.$	+ 14.0	- 29.	± 0.9	+ 73.	± 2	+ 44.

(f) The sizes of the nonlinear terms are not very sensitive to the eddy position (Tables IX and X).

In a statistical sense, the random eddy field spreads the perturbed rays about the interior of a ray tube (Figs. 9 and 10). The size of the ray tube increases as the eddies increase in strength. Sometimes, the initial ray is converted to a diffracted arrival (Fig. 10) where the ray does not pass through the receiver. This rarely occurs for the weaker eddy field whose anomalies are $\pm 1^\circ\text{C}$. (The ray paths are drawn between widely spaced points using linear interpolation. The ray trace program computes trajectories with much more accuracy than shown.)

The magnitude of Eq. (20) is about 1 ms (3 ms) for the $\pm 1^\circ\text{C}$ ($\pm 2^\circ\text{C}$) eddy field at a 1000-km range.

The change of the source angle between the perturbed and initial rays is as large as about 0.1° and 0.3° for the $\pm 1^\circ$ and $\pm 2^\circ\text{C}$ eddy fields (Table XI).

VII. 3000-km RANGE: SUBTROPICAL PACIFIC

Source and receiver are placed at axial depth (1.1 km) for the initial sound-speed profile (Fig. 7) at a 3000-km range. Initial travel times and geometries are computed for seven rays. They are + 116(413), + 120(458), + 124(498), + 128(527), + 132(551), + 136(573), + 140(595), and + 144(618).

The perturbed profile contains nine warm eddies and

nine cold eddies. The geometry of the eddy is the same as in Sec. VI.

One set of simulations is done. The eddies have maximum vertical water displacements of ± 50 m. Four realizations of the eddy field are constructed by mixing the orders and ranges of the eddies.

Exact travel times and geometries are computed for each realization for each of the seven rays. The results for two of the rays, + 116(413) and + 144(618), are typical. The conclusions are:

(a) The amount of the nonlinearity is large, as measured by e_2 (Table XII).

(b) δT_2 is not a consistently better estimator of δT_1 than is δT_3 (Table XII).

(c) The nonlinear terms δT_5 and δT_6 are usually of opposite signs (Table XIII).

(d) The magnitude of δT_6 usually exceeds the magnitude of δT_5 (Table XIII).

(e) The sum of the nonlinear terms is positive for six of the rays and negative for one of the rays (Table XIV).

(f) The sizes of the nonlinear terms are not sensitive to the positions of the eddies (Table XIV).

The perturbed ray paths for the four realizations show the size of the ray tube for this simulation (Fig. 11).

The size of the expression in Eq. (20) is about 3 ms for all the rays in this simulation.

The source angles typically change by 0.1° in this simulation (Table XV).

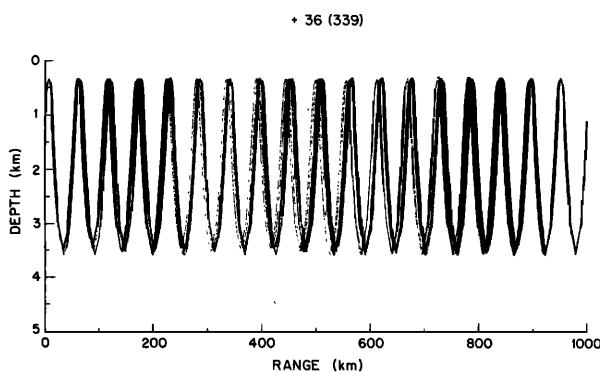


FIG. 9. The seven perturbed ray paths for the seven realizations of the eddy field for the simulated ocean in the subtropical Pacific. The eddies have maximum anomalies of $\pm 1^\circ\text{C}$.

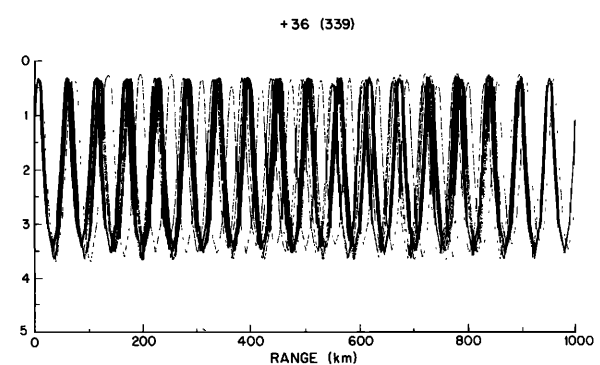


FIG. 10. Same as Fig. 9 except the eddies have maximum anomalies of $\pm 2^\circ\text{C}$. One of the rays is converted to a diffracted arrival and does not pass through the receiver.

TABLE XI. Standard deviations σ of source angles computed from seven realizations of the eddy field for the subtropical Pacific.

Identifier	Pacific, 1000-km range	
	$\pm 1^\circ\text{C}$ eddies σ (°)	$\pm 2^\circ\text{C}$ eddies σ
+ 36 (339)	0.03	0.05
+ 38 (398)	0.02	0.03
+ 40 (458)	0.01	0.05
+ 42 (515)	0.09	0.20
+ 44 (551)	0.20	0.30
+ 46 (584)	0.03	0.05
+ 48 (618)	0.03	0.07

VIII. BILINEAR MODEL

The question arises as to whether travel times computed for a simple model for mesoscale perturbations, which can be solved analytically, bear any resemblance to actual and simulated eddy fields previously investigated.

Consider an initial bilinear sound-speed profile given by

$$c_0(z) = \bar{c}(1 + \alpha_0^\pm |z - \bar{z}|), \quad (34)$$

where the sound speed at the axis \bar{z} is \bar{c} . α_0^+ applies above the axis and α_0^- applies below the axis. Let the perturbed sound-speed profile be

$$c_1(z) = \bar{c}(1 + \alpha_1^\pm |z - \bar{z}|). \quad (35)$$

Place a source and receiver at axis depth. The double-loop ranges for the initial and perturbed rays are given by

$$r_0 = |\tan \bar{\theta}_0| L_0, \quad (36)$$

$$r_1 = |\tan \bar{\theta}_1| L_1, \quad (37)$$

respectively, where

$$L_0 = 2(1/\alpha_0^+ + 1/\alpha_0^-), \quad (38)$$

$$L_1 = 2(1/\alpha_1^+ + 1/\alpha_1^-), \quad (39)$$

and where the axis angles of the unperturbed and perturbed rays are $\bar{\theta}_0$ and $\bar{\theta}_1$, respectively.

The travel times have the simplest form when the double-loop ranges of the unperturbed and perturbed rays are identical (phase locking). Then from Eqs. (36) and (37),

TABLE XII. Same as Table VIII except for a 3000-km range.

Realization	Pacific, 3000-km range $\pm 1^\circ\text{C}$ eddies + 116 (413)				
	δT_1 (ms)	δT_2	δT_3	e_2 (%)	e_3
1	-16.5	-0.4	-0.3	-98	-98
2	-15.1	-0.4	-0.3	-97	-98
3	-16.5	-1.9	-0.3	-88	-98
4	-14.4	+1.1	-0.3	-108	-98
+ 144 (618)					
1	+58.9	+17.3	+17.0	-71	-71
2	+55.6	+13.6	+17.0	-76	-69
3	+56.0	+14.8	+17.0	-74	-70
4	+57.3	+16.1	+17.0	-72	-70

$$\bar{\theta}_1 = \tan^{-1} [(L_0/L_1)\tan \bar{\theta}_0]. \quad (40)$$

For simplicity, the assumption is made that the perturbation is confined to be above the axis or

$$\alpha_1^- = \alpha_0^-. \quad (41)$$

Analytic expressions for δT_1 [Eq. (3)], δT_2 [Eq. (8)], δT_3 [Eq. (6)], and δT_6 [Eq. (9)] can be derived for a double-loop. They are (Appendix C)

$$\delta T_1 = \frac{1}{\bar{c}} \left[L_1 \ln \left(\frac{1 + |\sin \bar{\theta}_1|}{\cos \bar{\theta}_1} \right) - L_0 \ln \left(\frac{1 + |\sin \bar{\theta}_0|}{\cos \bar{\theta}_0} \right) \right], \quad (42)$$

$$\delta T_2 = \frac{2(\alpha_1^+/\alpha_0^+ - 1)}{\alpha_0^+ \bar{c}} \times \left[|\sin \bar{\theta}_0| - \ln \left(\frac{1 + \cos \bar{\theta}_0 + |\sin \bar{\theta}_0|}{1 + \cos \bar{\theta}_0 - |\sin \bar{\theta}_0|} \right) \right], \quad (43)$$

$$\delta T_5 = T_5 - (L_0/\bar{c}) \ln [(1 + |\sin \bar{\theta}_0|)/\cos \bar{\theta}_0], \quad (44)$$

$$\delta T_6 = \delta T_1 - \delta T_2 - \delta T_5. \quad (45)$$

The expression for T_5 can be expressed as contributions from quarter-loop segments. Let t_5 denote the contribution to T_5 from a ray between the axis to its turning point. Then

TABLE XIII. Same as Table IX except for a 3000-km range.

Realization	Pacific, 3000-km range $\pm 1^\circ\text{C}$ eddies + 116 (413)			
	δT_1 (ms)	δT_2	δT_5	δT_6
1	-16.5	-0.4	+10.9	-27.0
2	-15.1	-0.4	+11.2	-25.9
3	-16.5	-1.9	+11.2	-25.8
4	-14.4	+1.1	+11.3	-26.8
+ 144 (618)				
1	+58.9	+17.3	-29.3	+70.9
2	+55.6	+13.6	-29.4	+71.4
3	+56.0	+14.8	-28.8	+70.0
4	+57.3	+16.1	-29.1	+70.3

TABLE XIV. The means, standard deviations, and sums of the nonlinear terms for four realizations of the eddy field.

Initial ray	Pacific, 3000-km range ± 1 °C eddies				
	$\delta \bar{T}_5$ (ms)	σ	$\delta \bar{T}_6$	σ	$\delta \bar{T}_5 + \delta \bar{T}_6$
+ 116 (413)	+ 11.	± 0.2	- 26.	± 0.6	- 15.
+ 124 (498)	+ 1.6	± 0.5	+ 8.1	± 0.5	+ 9.7
+ 128 (527)	- 16.	± 2.	+ 27.	± 2.	+ 11.
+ 132 (551)	- 18.	± 2.	+ 33.	± 2.	+ 15.
+ 136 (573)	- 24.	± 0.2	+ 47.	± 0.6	+ 23.
+ 140 (595)	- 29.	± 0.3	+ 59.	± 0.6	+ 30.
+ 144 (618)	- 29.	± 0.3	+ 71.	± 0.6	+ 42.

TABLE XV. Standard deviations σ of source angles computed from four realizations of the eddy field for the subtropical Pacific.

Pacific, 3000-km range ± 1 °C eddies	
Identifier	σ (degrees)
+ 116 (413)	0.05
+ 120 (458)	...
+ 124 (498)	0.04
+ 128 (527)	0.1
+ 132 (551)	0.1
+ 136 (573)	0.04
+ 140 (595)	0.06
+ 144 (618)	0.1

$$t_s = \begin{cases} \frac{B^{-1/2}}{\bar{c} \cos \bar{\theta}_1} \ln \left(\frac{(1 + \cos \bar{\theta}_1)[\alpha_0 + (\alpha_1 - \alpha_0) \cos \bar{\theta}_1] + B^{1/2} \cos \bar{\theta}_1 |\sin \bar{\theta}_1|}{(1 + \cos \bar{\theta}_1)[\alpha_0 + (\alpha_1 - \alpha_0) \cos \bar{\theta}_1] - B^{1/2} \cos \bar{\theta}_1 |\sin \bar{\theta}_1|} \right), & B > 0; \\ \frac{2(-B)^{-1/2}}{\bar{c} \cos \bar{\theta}_1} \tan^{-1} \left(\frac{(-B)^{1/2} \cos \bar{\theta}_1 |\sin \bar{\theta}_1|}{(1 + \cos \bar{\theta}_1)[\alpha_0 + (\alpha_1 - \alpha_0) \cos \bar{\theta}_1]} \right), & B < 0; \\ |\tan \bar{\theta}_1| / [\bar{c}(\alpha_1 - \alpha_0)(1 + \cos \bar{\theta}_1)], & B = 0; \end{cases} \quad (46)$$

where

$$B = (\alpha_0 \tan \bar{\theta}_1)^2 + \alpha_1(2\alpha_0 - \alpha_1), \quad (47)$$

and one uses the + (−) superscript for quarter-loops above (below) the axis (Appendix C).

These exact expressions for the travel time changes are

now expanded in terms of the initial axis angle θ_0 and in terms of

$$\delta = \alpha_1^+ / \alpha_0^+ - 1, \quad (48)$$

using a computer program called MACSYMA.

For $|\delta| < 1$ and for each *double-loop*,

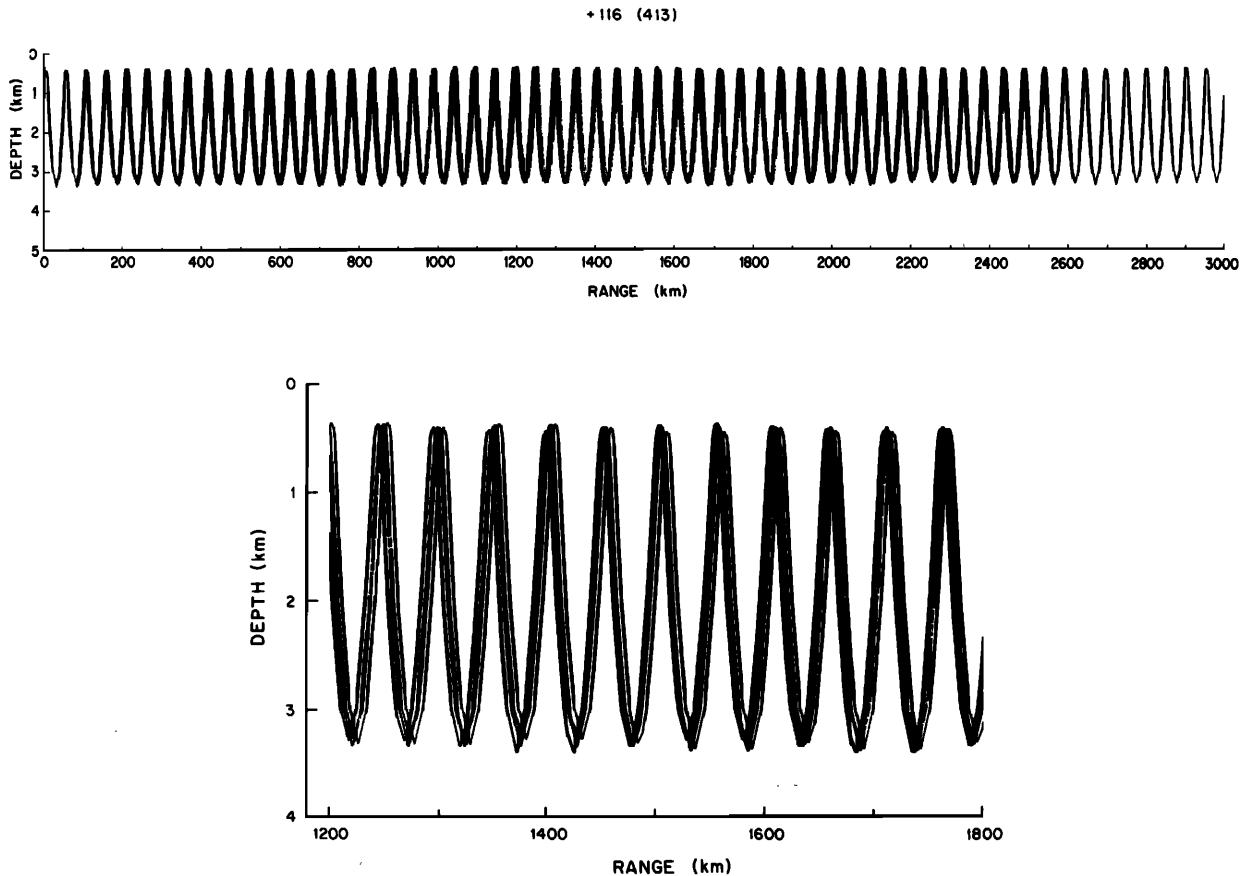


FIG. 11. The four perturbed ray paths for the four realizations of the eddy field for the simulated ocean in the subtropical Pacific. The eddies have maximum anomalies of ± 1 °C. The bottom panel is an enlargement of the central region.

$$\delta T_1 = \frac{-2}{3\alpha_0^+ \bar{c}} \left(\delta - \frac{(2\alpha_0^+ - \alpha_0^-)}{2(\alpha_0^+ + \alpha_0^-)} \delta^2 + \dots \right) |\bar{\theta}_0^3| \dots, \quad (49)$$

$$\delta T_2 = -(2\delta |\bar{\theta}_0^3| / 3\alpha_0^+ \bar{c}) + \dots, \quad (50)$$

$$\delta T_5 = \left(\frac{-(2\alpha_0^+ - \alpha_0^-) \delta^2}{3\alpha_0^+ (\alpha_0^+ + \alpha_0^-) \bar{c}} + \dots \right) |\bar{\theta}_0^3| + \dots, \quad (51)$$

$$\delta T_6 = 2 \left(\frac{(2\alpha_0^+ - \alpha_0^-) \delta^2}{3\alpha_0^+ (\alpha_0^+ + \alpha_0^-) \bar{c}} + \dots \right) |\bar{\theta}_0^3| + \dots. \quad (52)$$

These expressions all contain $\bar{\theta}_0^5$ as the next surviving term in the δT_2 variable $\bar{\theta}_0$ and so are much less than the terms in $\bar{\theta}_0^3$. The expression in Eq. (50) is exact in the variable δ .

The exact travel time change equals the linear change plus a nonlinear term equal to

$$\delta T_5 + \delta T_6 = \left(\frac{(2\alpha_0^+ - \alpha_0^-) \delta^2}{3\alpha_0^+ (\alpha_0^+ + \alpha_0^-) \bar{c}} + \dots \right) |\bar{\theta}_0^3| + \dots, \quad (53)$$

which is positive, zero, or negative depending on the value of $2\alpha_0^+ - \alpha_0^-$. (If a bilinear profile is used to model the sound-speed profiles shown in this paper then $2\alpha_0^+ > \alpha_0^-$.) The cubic term in δ is a factor of

$$-\delta \alpha_0^+ (\alpha_0^+ + \alpha_0^-) / [(\alpha_0^+)^2 + 2\alpha_0^- \alpha_0^+ + (\alpha_0^-)^2]$$

smaller than the quadratic term.

To estimate the size of the nonlinear term in Eq. (53) the values

$$\alpha_0^+ = 0.0294718 \text{ km}^{-1}, \quad \alpha_0^- = 0.0100402 \text{ km}^{-1},$$

$$\bar{c} = 1.48154 \text{ km/s}, \quad \bar{z} = 1.1 \text{ km},$$

are taken for the initial sound-speed profile (Fig. 7) which is a rough fit to the climatological profile near 30 °N and 145 °W in the Pacific. The exact expressions for δT_1 , δT_2 , δT_5 , and δT_6 per double-loop from Eqs. (42), (43), (44), and (45) are evaluated for an initial ray having a double-loop range of 50 km whose associated axis angle and upper turning depth is

$$\bar{\theta}_0 \simeq 10.6^\circ$$

and

$$z = 0.51 \text{ km}.$$

The Taylor expression for δT_1 has a negative slope and is quadratic, which causes the curve to be concave downward for $2\alpha_0^+ > \alpha_0^-$. δT_2 is linear in δ with no higher-order corrections. δT_5 and δT_6 are predicted to be quadratic in δ with δT_5 concave upwards and δT_6 concave downwards. These trends are all observed in the exact calculations shown in Fig. 12.

For these numbers, and for

$$\delta = \pm 0.184,$$

which corresponds to an equivalent temperature change of

$$\delta \theta = \pm 1^\circ \text{C}$$

at the upper turning depth for the unperturbed ray, the nonlinear terms are

$$2(\delta T_5 + \delta T_6) = 4 \text{ ms},$$

from Eq. (45) for *two* double-loops in a perturbed region of 100-km width. This scales as the square of δ , so for a temperature perturbation of $\pm 0.5^\circ \text{C}$, this estimate is multiplied by 0.25. For this model the relative contribution to the nonlinearity due to path changes below the axis is $\alpha_0^- / 2\alpha_0^+$.

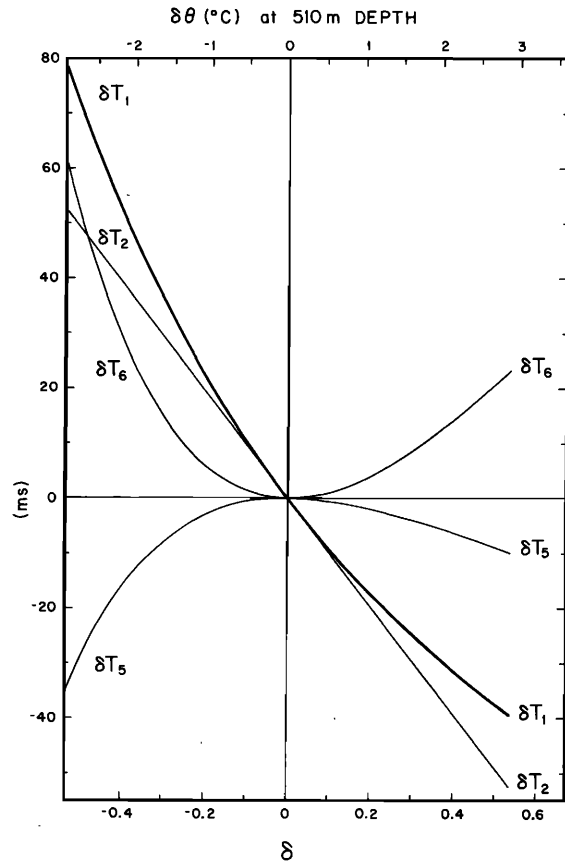


FIG. 12. Exact travel time calculations for the bilinear model for a ray with source angle equal to about 10.6°.

For the values from this example, this ratio equals 0.17 so that most of the nonlinearities accumulate above the axis.

Consider an equal number of warm and cold “eddies” of equal magnitude and opposite sign arranged so that the perturbation regions are integer multiples of the double-loop range and start and stop at the axis crossings (as before). Then δT_2 vanishes exactly and

$$\delta T_1 \simeq aR\delta^2 = \delta T_5 + \delta T_6, \quad (54)$$

where R is the total range and “ a ” is a constant. For this rather artificial model, the nonlinearities increase linearly with the range, quadratically with δ (or temperature) for small perturbations and are positive, negative, or zero depending on the sign of $2\alpha_0^+ - \alpha_0^-$.

IX. DISCUSSION

A. Vertical deflections of the ray path

In all of the numerical simulations studied here, the perturbed ray path drifts out of phase with the initial path and reaches a maximum shift at about one-half of the total range (Figs. 4, 9, and 10). The phase shift does not appear to be locally connected to any particular eddy. There is a local vertical deflection of the ray path associated with the eddies. For cold (warm) eddies the perturbed path is consistently elevated (lowered) at upper turning depths relative to the unperturbed path (not shown). The ray path separation function $\eta(x)$ is roughly periodic. Its wavelength is about equal to the double-loop range and its amplitude is small near the

TABLE XVI. The nonlinear terms and their sums for two unperturbed ray paths at 1000- and 3000-km ranges.

Pacific ± 1 °C eddies							
Initial ray	1000-km range $\delta T_5(\text{ms})$	$\delta \bar{T}_6$	$\delta \bar{T}_5 + \delta \bar{T}_6$	Initial ray	3000-km range δT_5	$\delta \bar{T}_6$	$\delta \bar{T}_5 + \delta \bar{T}_6$
+ 44 (551)	− 5.7	+ 10.	+ 4.3	+ 132 (551)	− 18.	+ 33.	+ 15.
+ 48 (618)	− 10.	+ 24.	+ 14.	+ 144 (618)	− 29.	+ 71.	+ 42.

source and receiver and reaches a maximum near the half-range point (Fig. 4). It appears that a serious shortcoming of the bilinear model is the insistence that the phase difference between the perturbed and unperturbed ray paths is not allowed to extend over more than a double-loop range. Extensions of the bilinear model which relax this restriction become an analytical nightmare.

Since the values of the nonlinear terms are relatively insensitive to changes of the eddy positions (Tables X and XIV), perhaps a stochastic formalism would yield fruitful results. If so, correlations of the quantities

$$\frac{\eta^2}{\cos \theta_0} \frac{\partial^2 n_0}{\partial z^2}, \quad n_0 \cos^3 \theta_0 \eta \frac{d^2 \eta}{dx^2}, \quad \frac{\eta}{\cos \theta_0} \frac{\partial(\delta n)}{\partial z},$$

may have to be derived as in Eqs. (24) and (25).

In spite of the restrictive nature of the bilinear model, we now check the numerical results to see if the nonlinear terms grow linearly with range and quadratically with temperature anomaly as in Eq. (54). The nonlinear terms for the Pacific approximately quadruple as the temperature anomaly increases from ± 1 to ± 2 °C except for one ray [+ 40(458)] (Table X). Furthermore, the signs of the nonlinear terms do not change sign. The nonlinear terms computed for the two rays whose unperturbed turning depths are identical are about three times larger at 3000-km ranges than at a 1000-km range (Table XVI). The signs of the nonlinear terms do not change as the range changes. It is remarkable that the bilinear model predicts a result which is approximately observed in the numerical calculations.

B. Horizontal deflections of the ray path

Let y be the coordinate perpendicular to the x - z plane in which the initial ray path lies. Suppose n_0 is a constant. Let $\gamma(x)$ denote the y separation between the ray and the x - z plane as a function of range. The general expansions for δT_5 and $\delta \bar{T}_6$ can be applied to yield

$$\delta T_5 \simeq \frac{-n_0}{2\bar{c}} \int_0^R dx \gamma \frac{d^2 \gamma}{dx^2} \quad (55)$$

and

$$\delta \bar{T}_6 \simeq \frac{1}{\bar{c}} \int_0^R dx \gamma \frac{\partial(\delta n)}{\partial y}. \quad (56)$$

These equations are valid to the same order as Eqs. (24) and (25).

Munk⁶ has computed the travel time due to horizontal path perturbation through a single eddy with no depth dependence. His expression for δT_1 and δT_2 is given by τ and τ_u , respectively [from Munk⁶ (12)], and the expression which

follows. Subtracting the expressions and using Munk's Eq. (5)⁶ yields

$$\delta T_5 + \delta \bar{T}_6 = 1.3 \times 10^{-5} R \delta \theta^2 \sin^2 \nu \cos^2 \nu, \quad (57)$$

where ν is the angle describing the angle at which the deflected ray enters the eddy. R is in km and $\delta \theta$ is in °C. Head-on incidence corresponds to $\nu = 90^\circ$ and tangential incidence corresponds to 0° . Equation (57) is valid for an eddy whose anomaly is independent of depth. To account for the decrease of the temperature anomaly with depth, Eq. (57) is multiplied by a constant less than unity (we will use 0.5). The average value for

$$\sin^2 \nu \cos^2 \nu$$

is 1/8. An average value for Eq. (57) modified for the depth dependence of an eddy is about

$$\delta T_5 + \delta \bar{T}_6 \simeq 8 \times 10^{-7} R \delta \theta^2. \quad (58)$$

For $R = 1000$ km and $\delta \theta = 1$ °C Eq. (58) is + 0.8 ms. For the Atlantic at 36 °N, the eddies have the same anomaly and the nonlinear terms have values from − 2.1 through − 21.6 ms (Table XI). The value for the horizontal deflection needs to be increased by some amount for a field of eddies. As Munk⁶ has suggested, three-dimensional ray tracing should be used to measure the effects of horizontal deflections.

It is intriguing that the forms for the nonlinear terms for horizontal deflections [Eq. (58)] and for the vertical deflections for the bilinear model [Eq. (54)] are identical.

C. Comments on inverse procedures

For acoustic transmissions over long ranges in the ocean, an experimenter usually computes initial travel times from a climatological sound-speed profile where the features due to eddies are greatly reduced through averaging historical measurements. One then measures travel times for various ray paths and computes δT_1 for each ray. If the δT_1 are used as the data for *linear* inversion schemes, the estimates will be biased. For example, at 24 °N in the east Atlantic, the nonlinear terms are positive. If δT_2 is used to model δc and δT_2 is replaced with the measured δT_1 , one will obtain a sound-speed (temperature) fluctuation relative to the initial state that is less than the actual fluctuation. An ocean that is colder than reality would be inferred. On the other hand, at 36 °N in the east Atlantic, the sums of the nonlinear terms are negative and a *linear* inversion scheme will result in an ocean that is warmer than reality. The bias depends on the climatological profile for the region and on the set of rays chosen for the inversion.

Linear inversion schemes allow computations of the misfit between the measured data and data predicted from

the estimates. If one weights the travel time data according to a random uncertainty whose size is equal to the size of the nonlinear terms, a consistent model will be estimated. However, if the data are weighted according to the precision of the travel time measurement, unreasonable residuals will appear.

Another approach is to iterate linearized models. Further analysis of the horizontal deflection problem should be done to determine whether it is necessary to iterate three-dimensional models. When the nonlinearities are not large, as at 24 °N in the Atlantic, iteration may provide correct results. It is more uncertain whether iterations will provide correct results for larger nonlinearities such as those found at 36 °N in the Atlantic.

Another approach is to estimate the size of the nonlinear terms from an *a priori* knowledge of the eddy spectrum. The terms could be computed using a two- or three- (if necessary) dimensional ray trace program. Once the size of the nonlinear terms is known, they can be subtracted from the δT_1 to estimate the $\delta \tilde{T}_2$. The $\delta \tilde{T}_2$ can then be used in a linear inversion scheme which is two-dimensional and which requires no iteration.

ACKNOWLEDGMENTS

Steven Bellerose helped with the computer calculations. Carl Wunsch and Dean Roemmick generously provided the hydrographic measurements in the Atlantic. The analytical expansions for the bilinear profile were computed with a program called MACSYMA written by the Math lab group at MIT. The Math lab group is supported in part by the National Aeronautics and Space Administration under grant NSG1323, by the Office of Naval Research under grant N00014-77-C-0641, by the U. S. Department of Energy under grant ET-78-C-02-4687, and by the U. S. Air Force under grant F49620-79-C-020. The work in this paper is supported by the Office of Naval Research under contract N00014-82-C-0019 and by the National Science Foundation under grant OCE-80-17309. W. H. O. I. contribution number 5722.

APPENDIX A: INDEX OF REFRACTION MODELS

A. Relations between sound speed and index of refraction models

The initial travel time is

$$T_0 = \frac{1}{\bar{c}} \int_{r_1} ds n_0, \quad (A1)$$

where

$$n_0 = \bar{c}/c_0(x, z) \quad (A2)$$

is the initial index of refraction. The exact travel time for a perturbed state is

$$T_1 = \frac{1}{\bar{c}} \int_{r_1} ds (n_0 + \delta n). \quad (A3)$$

Then

$$\delta T_1 = \frac{1}{\bar{c}} \int_{r_1} ds (n_0 + \delta n) - \frac{1}{\bar{c}} \int_{r_0} ds n_0,$$

or

$$\delta T_1 = \delta T_5 + \frac{1}{\bar{c}} \int_{r_1} ds \delta n, \quad (A4)$$

where

$$\delta T_5 = \frac{1}{\bar{c}} \left(\int_{r_1} ds n_0 - \int_{r_0} ds n_0 \right). \quad (A5)$$

Also,

$$\frac{1}{\bar{c}} \int_{r_1} ds \delta n = \delta \tilde{T}_2 + \delta \tilde{T}_6, \quad (A6)$$

where

$$\delta \tilde{T}_2 = \frac{1}{\bar{c}} \int_{r_0} ds \delta n(x, z) \quad (A7)$$

and

$$\delta \tilde{T}_6 = \frac{1}{\bar{c}} \left(\int_{r_1} ds \delta n - \int_{r_0} ds \delta n \right). \quad (A8)$$

Then

$$\delta T_1 = \delta \tilde{T}_2 + \delta T_5 + \delta \tilde{T}_6, \quad (A9)$$

where $\delta \tilde{T}_2$ is linear in the model δn and δT_5 and $\delta \tilde{T}_6$ are nonlinear in the model δn . $\delta \tilde{T}_2$ and δT_2 are closely related. Using

$$n_0 + \delta n = \bar{c}/(c_0 + \delta c), \quad (A10)$$

one obtains

$$\delta \tilde{T}_2 = \delta T_2 + \int_{r_0} \frac{ds \delta c^2}{c_0^2 (c_0 + \delta c)}, \quad (A11)$$

and

$$\delta \tilde{T}_6 = \delta T_6 - \int_{r_0} \frac{ds \delta c^2}{c_0^2 (c_0 + \delta c)}. \quad (A12)$$

B. Expansion for δT_5

From Eq. (A5),

$$\delta T_5 = \frac{1}{\bar{c}} \left(\int_0^R dx \mathcal{L}(z_1, z'_1; x) - \int_0^R dx \mathcal{L}(z_0, z'_0; x) \right), \quad (A13)$$

where

$$\cos \theta = \frac{dx}{ds}, \quad (A14)$$

and where

$$\mathcal{L}(z, z'; x) = (1 + z'^2)^{1/2} n_0(x, z) \quad (A15)$$

is the classical Lagrangian. Also,

$$z' = \frac{dz}{dx}, \quad (A16)$$

and the range between source and receiver is R . The subscripts 0 and 1 in Eq. (A13) denote that the variable is evaluated along the initial and perturbed ray paths, respectively.

The Lagrangian is now expanded about the initial ray path in the variables $\eta(x)$ and $d\eta/dx$, as in the calculus of variations. Here, $\eta(x)$ is the vertical distance between the initial ray path and another as yet arbitrary path which also intersects the source and receiver. Then

$$\begin{aligned}\mathcal{L}(z_1, z'; x) = \mathcal{L}(z_0, z'_0; x) + \frac{\partial \mathcal{L}}{\partial z} \Big|_{z_0} \eta(x) + \frac{\partial \mathcal{L}}{\partial z'} \Big|_{z_0} \frac{d\eta}{dx} + \frac{1}{2} \frac{\partial^2 \mathcal{L}}{\partial z^2} \Big|_{z_0} \eta^2 + \frac{\partial^2 \mathcal{L}}{\partial z \partial z'} \Big|_{z_0} \eta \frac{d\eta}{dx} + \frac{1}{2} \frac{\partial^2 \mathcal{L}}{\partial z'^2} \Big|_{z_0} \left(\frac{d\eta}{dx} \right)^2 \\ + \frac{1}{6} \frac{\partial^3 \mathcal{L}}{\partial z^3} \Big|_{z_0} \eta^3 + \frac{1}{2} \frac{\partial^3 \mathcal{L}}{\partial z^2 \partial z'} \Big|_{z_0} \eta^2 \frac{d\eta}{dx} + \frac{1}{2} \frac{\partial^3 \mathcal{L}}{\partial z \partial z'^2} \Big|_{z_0} \eta \left(\frac{d\eta}{dx} \right)^2 + \frac{1}{6} \frac{\partial^3 \mathcal{L}}{\partial z'^3} \Big|_{z_0} \left(\frac{d\eta}{dx} \right)^3 + \dots\end{aligned}\quad (\text{A17})$$

The vertical lines in Eq. (A17) mean that the preceding term is evaluated along the initial ray path. After the appropriate derivatives are calculated, the expression for $\mathcal{L}(z, z'; x)$ from Eq. (A17) is substituted into Eq. (A13), which yields

$$\begin{aligned}\delta T_5 = \frac{1}{c} \int_0^R dx \left[\frac{\partial^2 n_0}{\partial z^2} \frac{\eta^2}{2 \cos \theta_0} + \frac{\partial n_0}{\partial z} \sin \theta_0 \eta \frac{d\eta}{dx} + \frac{n_0 \cos^3 \theta_0}{2} \left(\frac{d\eta}{dx} \right)^2 + \frac{\partial^3 n_0}{\partial z^3} \frac{\eta^3}{6 \cos \theta_0} \right. \\ \left. + \frac{\sin \theta_0}{2} \frac{\partial^2 n_0}{\partial z^2} \eta^2 \frac{d\eta}{dx} + \frac{\partial n_0}{\partial z} \frac{\cos^3 \theta_0 \eta}{2} \left(\frac{d\eta}{dx} \right)^2 - \frac{n_0 \sin \theta_0 \cos^4 \theta_0}{2} \left(\frac{d\eta}{dx} \right)^3 + \dots \right].\end{aligned}\quad (\text{A18})$$

This expression is accurate through the first two orders of the terms which survive. The zero-order term cancels with the second integral in Eq. (A13). Because the integrand for the first integral in Eq. (A13) is the Lagrangian, the first-order terms vanish by Fermat's principle. (Snell's law is a result of the vanishing of the first-order terms.) Then, the expression for δT_5 in Eq. (A18) contains second- and third-order terms.

Equation (A18) can be integrated by parts to obtain

$$\begin{aligned}\delta T_5 = \frac{1}{2c} \int_0^R dx \eta^2 \left[\frac{1}{\cos \theta_0} \frac{\partial^2 n_0}{\partial z^2} + 3 \cos \theta_0 \left(\frac{\partial \cos \theta_0}{\partial x} \right)^2 n_0 - \frac{\partial \sin \theta_0}{\partial x} \frac{\partial n_0}{\partial z} + \frac{3}{2} \cos^2 \theta_0 \frac{\partial^2 \cos \theta_0}{\partial x^2} n_0 \right. \\ \left. + 3 \cos^2 \theta_0 \frac{\partial \cos \theta_0}{\partial x} \frac{\partial n_0}{\partial z} - \sin \theta_0 \frac{\partial^2 n_0}{\partial x \partial z} + \frac{\cos^3 \theta_0}{2} \frac{d^2 n_0}{dx^2} + \dots \right] - \frac{1}{2c} \int_0^R dx n_0 \cos^3 \theta_0 \eta \frac{d^2 \eta}{dx^2} + \dots,\end{aligned}\quad (\text{A19})$$

which is carried out here for the second-order terms. In general, all the terms in Eq. (A18) can be written as a product of η times some expression, through a suitable integration by parts. Therefore, the integrand vanishes when η vanishes.

C. Expansion for $\delta \tilde{T}_6$

From Eq. (A8),

$$\delta \tilde{T}_6 = \frac{1}{c} \left(\int_0^R dx \mathcal{M}(z_1, z'_1; x) - \int_0^R dx \mathcal{M}(z_0, z'_0; x) \right), \quad (\text{A20})$$

where

$$\mathcal{M}(z, z'; x) = (1 + z'^2)^{1/2} \delta n(x, z). \quad (\text{A21})$$

The function \mathcal{M} is now expanded about the initial ray path as is done for the function \mathcal{L} in Eq. (A17). When the suitable derivatives of \mathcal{M} are calculated the result is

$$\begin{aligned}\delta \tilde{T}_6 = \frac{1}{c} \int_0^R dx \left[\frac{1}{\cos \theta_0} \eta \frac{\partial(\delta n)}{\partial z} + \sin \theta_0 \delta n \frac{d\eta}{dx} \right. \\ \left. + \frac{1}{2 \cos \theta_0} \frac{\partial^2(\delta n)}{\partial z^2} \eta^2 + \sin \theta_0 \frac{\partial(\delta n)}{\partial z} \eta \frac{d\eta}{dx} \right. \\ \left. + \frac{\cos^3 \theta_0}{2} \delta n \left(\frac{d\eta}{dx} \right)^2 + \dots \right].\end{aligned}\quad (\text{A22})$$

The zero-order term in the expansion for \mathcal{M} cancels with the second integral in Eq. (A20). This time, however, the first-order terms for \mathcal{M} do not vanish since \mathcal{M} is not the Lagrangian. Thus Eq. (A22) contains the first- and second-order terms. In Eq. (A22), δn is evaluated along the initial ray path.

Equation (A22) can be integrated by parts to obtain

$$\begin{aligned}\delta \tilde{T}_6 = \frac{-1}{c} \int_0^R dx \eta \left(\frac{-1}{\cos \theta_0} \frac{\partial(\delta n)}{\partial z} \right. \\ \left. + \frac{\partial \sin \theta_0}{\partial x} \delta n + \sin \theta_0 \frac{\partial(\delta n)}{\partial x} + \dots \right),\end{aligned}\quad (\text{A23})$$

which includes only the first-order terms of Eq. (A22). All

the higher-order terms in Eq. (A22) can be integrated by parts so that η multiplies some expression. Therefore, when η vanishes, so does the integrand for $\delta \tilde{T}_6$.

APPENDIX B: SIZES OF TERMS FROM THE EXPANSION FOR THE OCEAN

A. δT_5

In order to estimate the orders of the terms in Eq. (21), results from unrelated physical examples are used. Consider a ray path for a bilinear sound-speed profile as in Eq. (30). The ray paths are sections of circles which obey the following:

$$\frac{\partial \sin \theta_0}{\partial x} = \frac{\pm 1}{R^\pm}, \quad (\text{B1})$$

$$\frac{\partial \cos \theta_0}{\partial x} = \frac{\pm \tan \theta_0}{R^\pm}, \quad (\text{B2})$$

$$\frac{\partial^2 \cos^2 \theta_0}{\partial x^2} = \frac{-(2 \cos^2 \theta_0 + 1)}{(R^\pm)^2 \cos^3 \theta_0}, \quad (\text{B3})$$

where

$$R^\pm = \frac{1}{\alpha_0^\pm \cos \bar{\theta}_0} \quad (\text{B4})$$

is the radius of curvature.

A canonical profile for the index of refraction is

$$n_0(z) = [1 + \epsilon(\beta + e^{-\beta} - 1)]^{-1}, \quad (\text{B5})$$

where

$$\beta = 2(\bar{z} - z)/B, \quad (\text{B6})$$

and z is positive upwards and zero at the axis (Munk⁸). Then

$$\frac{\partial n_0}{\partial z} = \frac{-2\epsilon n_0^2}{B} (1 - e^{-\beta}) \quad (\text{B7})$$

and

$$\frac{\partial^2 n_0}{\partial z^2} = \frac{-4\epsilon}{B^2} n_0^2 [e^{-\beta}(1 + 4\epsilon n_0) - 2\epsilon n_0(1 + e^{-2\beta})]. \quad (B8)$$

To estimate the size of the second integral in Eq. (21), consider a simple model such as

$$\eta(x) = A [\cos(kx - \phi_1) - \cos(kx - \phi_2)]. \quad (B9)$$

For simplicity, A , k , ϕ_1 , and ϕ_2 are constants. Then

$$\frac{d^2 \eta}{dx^2} = -k^2 \eta. \quad (B10)$$

In order to evaluate the orders of magnitude for the terms in Eq. (21), the following values are taken:

$$\epsilon = 7.4 \times 10^{-3}, \quad \beta = 1 \text{ km}.$$

Then

$$\frac{\eta^2}{2\bar{c} \cos \theta_0} \frac{\partial^2 n_0}{\partial z^2} \sim \frac{-2\epsilon}{\bar{c}} e^{-\beta} \eta^2, \quad (B11)$$

$$\frac{\eta^2}{2\bar{c}} \frac{\partial \sin \theta_0}{\partial x} \frac{\partial n_0}{\partial z} \sim \frac{\pm \epsilon(1 - e^{-\beta})}{\bar{c} R^{\pm}} \eta^2, \quad (B12)$$

$$\frac{3\eta^2}{2\bar{c}} \cos \theta_0 \left(\frac{\partial \cos \theta_0}{\partial x} \right)^2 n_0 \sim \frac{3 \tan^2 \theta_0 \eta^2}{2\bar{c}(R^{\pm})^2}, \quad (B13)$$

$$\eta^2 \frac{3 \cos^2 \theta_0}{4\bar{c}} \frac{\partial^2 \cos \theta_0}{\partial x^2} n_0 \sim \frac{-5\eta^2}{2\bar{c}(R^{\pm})^2}, \quad (B14)$$

$$\frac{n_0 \cos^3 \theta_0}{2\bar{c}} \eta \frac{d^2 \eta}{dx^2} \sim -\frac{k^2 \eta^2}{2\bar{c}}, \quad (B15)$$

where the values,

$$n_0 \sim 1, \quad \cos \theta_0 \sim 1,$$

have been used. Typical values for these numbers are

$$\bar{c} = 1.5 \text{ km/s},$$

$$R^+ = 31 \text{ km}, \quad R^- = 93 \text{ km}, \quad \theta_0 = 0.1 \text{ rad},$$

$$\beta = \begin{cases} -1 & \text{above the axis,} \\ 0 & \text{at the axis,} \\ 2 & \text{below the axis,} \end{cases}$$

$$k = 2\pi/50 \text{ km}.$$

The sizes of the terms for these values are shown in Table I.

B. $\delta \bar{T}_e$

Using Eqs. (27) and (A10),

$$\delta n \cong -3 \times 10^{-3} \delta \theta, \quad (B16)$$

where $\delta \theta$ is interpreted here as the maximum temperature anomaly due to a mesoscale eddy. Typical values for the vertical derivative of δn for an eddy are

$$\frac{\partial(\delta n)}{\partial z} \sim \begin{cases} (3 \times 10^{-3} \delta \theta)/0.5 \text{ km}^{-1}, & \text{above axis} \\ (3 \times 10^{-3} \delta \theta)/1 \text{ km}^{-1}, & \text{at axis} \\ 0, & \text{below axis.} \end{cases}$$

Typical values for the horizontal derivative of δn for an eddy are

$$\frac{\partial(\delta n)}{\partial x} \sim \begin{cases} [(3 \times 10^{-3})/40] \delta \theta \text{ km}^{-1}, & \text{above axis} \\ [(3 \times 10^{-3})/80] \delta \theta \text{ km}^{-1}, & \text{at axis} \\ 0, & \text{below axis.} \end{cases}$$

Then,

$$\frac{\eta}{\bar{c}} \frac{\partial \sin \theta_0}{\partial x} \delta n \sim \frac{3 \times 10^{-3}}{\bar{c} R^{\pm}} \eta \delta \theta, \quad (B17)$$

$$\frac{\eta}{\bar{c} \cos \theta_0} \frac{\partial(\delta n)}{\partial z} \sim \frac{\eta}{\bar{c}} \frac{\partial(\delta n)}{\partial z}, \quad (B18)$$

$$\frac{\eta}{\bar{c}} \sin \theta_0 \frac{\partial(\delta n)}{\partial x} \sim \frac{\eta \sin \theta_0}{\bar{c}} \frac{\partial(\delta n)}{\partial x}. \quad (B19)$$

As before the following values are taken:

$$\bar{c} = 1.5 \text{ km/s}, \quad R^+ = 31 \text{ km},$$

$$R^- = 93 \text{ km}, \quad \theta_0 = 0.1 \text{ rad}.$$

The sizes of the terms in Eqs. (B17)–(B19) are evaluated in Table I.

APPENDIX C. BILINEAR MODEL

The vertical coordinate is positive upwards and x is the range coordinate. The ray angle with respect to the horizontal is defined through

$$\tan \theta = \frac{dz}{dx}. \quad (C1)$$

For a sound-speed field which is independent of the range coordinate Snell's law is

$$\cos \theta(x, z)/c(z) = 1/\hat{c}, \quad (C2)$$

where \hat{c} is the speed of sound at the upper or lower turning depth where the ray angle vanishes. Since

$$\tan \theta = (1/\cos^2 \theta - 1)^{1/2}, \quad (C3)$$

and from (C2),

$$\cos \theta = c(z)/\hat{c}, \quad (C4)$$

Eq. (C1) can be solved for x through integration, which yields

$$x = \int dz \left(\frac{\hat{c}^2}{c^2(z) - 1} \right)^{-1/2}. \quad (C5)$$

For the bilinear profile given by Eqs. (34) or (35) the ray paths are circular arcs with radius

$$\rho_i = 1/(\alpha_i^{\pm} \cos \bar{\theta}_i); \quad i = 0, 1, \quad (C6)$$

centered at a depth

$$z_0 = \bar{z} \pm 1/\alpha_i^{\pm}; \quad i = 0, 1. \quad (C7)$$

The double-loop ranges are given by Eqs. (36) and (37). The depth of the ray can be expressed in terms of the ray angle using

$$z = \begin{cases} z_0 - \rho \cos \theta, & z > \bar{z}, \\ z_0 + \rho \cos \theta, & z < \bar{z}. \end{cases} \quad (C8)$$

The unperturbed and perturbed travel times are found from

$$T_i = \int \frac{ds}{c_i(z)}, \quad (C9)$$

where ds is an increment of arc length and equals

$$ds = \rho d\theta. \quad (C10)$$

The double-loop travel times for the unperturbed and perturbed rays are

$$T_i = (1/\bar{c}) L_i \ln[(1 + |\sin \bar{\theta}_i|)/\cos \bar{\theta}_i]; \quad i = 0, 1. \quad (C11)$$

The integral for δT_2 per quarter-loop can be written as

$$\delta T_2(\text{q. loop}) = -\rho_0 I, \quad (\text{C12})$$

where

$$I = \int_0^{|\bar{\theta}_0|} \frac{\delta c \, d\theta}{c_0^2} \quad (\text{C13})$$

and

$$\delta c = c_1 - c_0. \quad (\text{C14})$$

The integral for I in (C13) can be written as

$$I = a_1 I_1 + a_2 I_2, \quad (\text{C15})$$

where

$$a_1 = \bar{c}(1 - \alpha_1^\pm / \alpha_0^\pm), \quad (\text{C16})$$

$$a_2 = \bar{c}(\alpha_1^\pm / \alpha_0^\pm - 1) / \cos \bar{\theta}_0, \quad (\text{C17})$$

$$I_1 = \int_0^{|\bar{\theta}_0|} \frac{d\theta}{(d_2 \cos \theta)^2}, \quad (\text{C18})$$

$$I_2 = \int_0^{|\bar{\theta}_0|} \frac{d\theta \cos \theta}{(d_2 \cos \theta)^2}, \quad (\text{C19})$$

$$d_2 = \bar{c} / \cos \bar{\theta}_0. \quad (\text{C20})$$

Now

$$I_2 = \frac{1}{d_2} \frac{\cos \bar{\theta}_0}{\bar{c}} \ln \left(\frac{1 + \tan(|\bar{\theta}_0|/2)}{1 - \tan(|\bar{\theta}_0|/2)} \right) \quad (\text{C21})$$

and

$$J = \begin{cases} (g^2 - f^2)^{-1/2} \ln \left(\frac{(g^2 - f^2)^{1/2} \tan(\theta/2) + f + g}{-(g^2 - f^2)^{1/2} \tan(\theta/2) + f + g} \right) \Big|_0^{|\bar{\theta}|}, & f^2 - g^2 < 0, \\ (1/f) \tan(\theta/2) \Big|_0^{|\bar{\theta}|}, & f = g, \\ 2(f^2 - g^2)^{-1/2} \tan^{-1} \left(\frac{(f^2 - g^2)^{1/2} \tan(\theta/2)}{f + g} \right) \Big|_0^{|\bar{\theta}|}, & f^2 - g^2 > 0. \end{cases} \quad (\text{C29})$$

With B defined as in (47), the expressions in (47) follow from (C29). The expression for δT_6 is obtained from (10).

$$I_1 = |\sin \bar{\theta}_0| \cos \bar{\theta}_0 / \bar{c}^2. \quad (\text{C22})$$

Using the identity

$$\tan \gamma/2 = \sin \gamma / (1 + \cos \gamma), \quad (\text{C23})$$

yields

$$I = \frac{(1 - \alpha_1^\pm / \alpha_0^\pm)}{\bar{c}} \cos \bar{\theta}_0 \left[|\sin \bar{\theta}_0| - \ln \left(\frac{1 + \cos \bar{\theta}_0 + |\sin \bar{\theta}_0|}{1 + \cos \bar{\theta}_0 - |\sin \bar{\theta}_0|} \right) \right] \quad (\text{C24})$$

from which Eq. (43) follows for a double-loop with Eq. (41).

The integral for T_5 per quarter-loop is

$$T_5(\text{q. loop}) = \rho_1 J, \quad (\text{C25})$$

$$J = \int_0^{|\bar{\theta}_1|} \frac{d\theta_1}{c_0}, \quad (\text{C26})$$

where the integral is along the angle of the perturbed path.

Define

$$f = \bar{c}(1 - \alpha_0^\pm / \alpha_1^\pm) \quad (\text{C27})$$

and

$$g = (\bar{c} / \cos \bar{\theta}_1)(\alpha_0^\pm / \alpha_1^\pm). \quad (\text{C28})$$

Then

¹J. L. Spiesberger, T. G. Birdsall, and K. Metzger, "Stability and identification of long range ocean acoustic multipaths," *J. Acoust. Soc. Am.* **67**, 2011–2017 (1980).

²J. L. Spiesberger, T. G. Birdsall, K. Metzger, R. A. Knox, C. W. Spofford, and R. C. Spindel, "Measurements of Gulf Stream meandering and evidence of seasonal thermocline development using long range acoustic transmissions," *J. Phys. Ocean.* **13**(10), 1836–1846 (1983).

³W. H. Munk and C. Wunsch, "Up-down resolution in ocean acoustic tomography," *Deep Sea Res.* **29**, no. 12a, 1415–1436 (1982).

⁴B. C. Cornuelle, "Acoustic tomography," *IEEE Trans. Geosci. Remote Sensing* **GE-20**(3) (1982).

⁵J. L. Spiesberger and P. F. Worcester, "Perturbations in travel time and ray geometry due to mesoscale disturbances: A comparison of exact and approximate calculations," *J. Acoust. Soc. of Am.* **74**, 219–225 (1983).

⁶W. H. Munk, "Horizontal deflection of acoustic ray paths by mesoscale eddies," *J. Phys. Ocean.* **10**(4), (1980).

⁷J. G. Richman, C. Wunsch, and N. Hogg, "Space and time scales of mesoscale motion in the western North Atlantic," *Rev. Geophys. Space Phys.* **15**, 385–420 (1977).

⁸W. H. Munk, "Sound channel in an exponentially stratified ocean, with application to SOFAR," *J. Acoust. Soc. Am.* **55**, 220–226 (1974).